Modeling electrochemical CO_2 reduction reaction on transition metal oxides

Narges Atrak

Faculty of Industrial Engineering, Mechanical Engineering and Computer Science
University of Iceland
2023

Modeling electrochemical CO_2 reduction reaction on transition metal oxides

Narges Atrak

Dissertation submitted in partial fulfillment of a
Philosophiae Doctor degree in Chemical Engineering

Advisor
Prof. Egill Skúlason

PhD Committee
Prof. Egill Skúlason
Prof. Hannes Jónsson
Dr. Elvar Örn Jónsson

Opponents
Prof. Anders Hellman
Dr. Federico Calle-Vallejo

Faculty of Industrial Engineering, Mechanical Engineering
and Computer Sciences
University of Iceland
Reykjavik, March 2023

Modeling electrochemical CO_2 reduction reaction on transition metal oxides.
Dissertation submitted in partial fulfillment of a *Philosophiae Doctor* degree in Chemical Engineering

Faculty of Industrial Engineering, Mechanical Engineering
and Computer Sciences
School of Engineering and Natural sciences
University of Iceland
Tæknigarði, Dunhaga 5
107, Reykjavik
Iceland

Telephone: 525 4000

Bibliographic information:
Narges Atrak, 2023, Modeling electrochemical CO_2 reduction reaction on transition metal oxides, PhD dissertation, Faculty of Industrial Engineering, Mechanical Engineering and Computer Sciences,
University of Iceland, 158 pp.

Author ORCID: 0000-0002-3108-5735

Printing: Háskólaprent, Fálkagata 2, 107 Reykjavík
Reykjavik, Iceland, March 2023

Abstract

The main target of this thesis is to use density functional theory (DFT)-based simulations to study electrochemical CO_2 reduction reactions (CO_2RR) on transition metal oxides (TMOs) employing thermochemical model and computational hydrogen electrode. We utilize models of rutile oxide (110) surfaces to investigate trends and limitations of CO_2RR on those TMOs. We construct scaling law based thermodynamic volcano relation for CO_2RR. Accordingly, we propose guidelines for hydrogen and OH binding free energy range where low overpotentials and high selectivity are predicted for CO_2RR using certain oxides. Therefore, this provides guidance to future development of oxide catalysts for CO_2RR. First, we investigate the effect of solvent on the stability of intermediates in CO_2RR toward methanol and formic acid formation and the competing hydrogen evolution reaction (HER). To study the solvent effect, one monolayer of water is included in the free energy calculations of adsorbates in CO_2RR and HER and compared with the results when water is absent. The emphasis is on the catalytic trends where limiting potential volcano plots for the products are obtained through the scaling relations of adsorbates. We find that the presence of cooperative adsorbed (co-adsorbed) water alters the interaction between each CO_2RR intermediate and TMO surfaces, resulting in a change in overpotentials for the formation of formic acid and methanol, ranging from 0.2 to 0.5 V while the potential determining steps remain unaltered. In addition, our research reveals that when water is co-adsorbed, it destabilizes HCOOH on surfaces which is significant because HCOOH is a crucial component for CO_2RR to advance toward methanol production. Consequently, this destabilization alters the selectivity of methanol formation. Furthermore, we conducted a comprehensive study to investigate oxygen, carbon, and hydrogen affinities for TMOs and their roles in catalyst's activity and selectivity. Our results are in good agreement with a recent experimental finding on RuO_2-based catalysts where both CO and formate products are detected with quite low efficiencies and HER is reported to be dominant. Our detailed investigation shows that the CO coverage has a considerable influence on the selectivity. For all TMOs in this investigation, moderate CO coverage is desirable for both formic acid and methanol synthesis. Additionally, MoO_2 and HfO_2 are predicted to convert CO_2 to methanol at lower overpotentials with moderate or high CO coverage than low coverage. Moreover, our data indicate that increased CO coverage on TMOs can lower HER somewhat. The research also highlights the significance of understanding the multiple adsorption sites and their correlation with active and selective catalysts for the synthesis of methanol from CO_2RR using the proper screening criteria for the adsorption energy of the key intermediates. The outcome of these investigations has led us to our final work where we analyze and identify the active sites for CO_2RR towards CO and formic acid on TiO_2/RuO_2 and SnO_2/RuO_2 alloys using DFT. To determine experimental trends and to gain insights into the catalytic active sites, Ru atoms are substituted in varying ratios and compositions for Ti and Sn atoms in TiO_2 and SnO_2 respectively. We found that alternate Ru-Ti binding sites for COOH/OCHO intermediates have higher overpotentials than the reference RuO_2 surface, while active sites with Ru-Ru or Ti-Ti exhibit lower overpotentials for CO formation. For formic acid formation, Ru-Ru sites have the lowest overpotentials, whereas Ti-Ti binding sites result in large overpotentials. We also discovered that replacing one Ru

atom with Cu in a RuO_2 overlayer on TiO_2 reduces the overpotential for both formic acid and CO formation. Additionally, substituting Sn with Ru in coordinatively unsaturated sites of SnO_2/RuO_2 alloys decreases the overpotential due to electronic effects. These findings are useful for designing active sites for CO_2RR, improving selectivity while decreasing the required overpotential.

Útdráttur

Megin markmið doktorsritgerðarinnar er að nota tölvureikninga byggða á þéttnifellafræði til að rannsaka CO_2 afoxun á málmoxíðum með varmafræðilegu líkani sem og líkani fyrir vetnis hálfskaut. Yfirborðin eru með rutile oxíð (110) byggingu og eru notuð til að rannsaka hneigð og tamkarkandi þætti fyrir CO_2 afoxun. Varmafræðilegar eldfjallamyndir eru búnar til frá línulegum samböndum á milli bindiorka milliástanda í CO_2 hvarfinu. Með þessari aðferð leggjum við til leiðarvísa fyrir bindingu á vetnisatómi og OH sameindum þar sem lág yfirspenna og há nýtni er spáð fyrir CO_2 afoxun á ákveðnum oxíðum. Þetta gerir okkur kleift að þróa betri efnahvata byggða á málmoxíðum fyrir CO_2 afoxun. Fyrst eru áhrif frá vatnssameindum rannsökuð fyrir stöðugleika milliástanda í CO_2 afoxun í metanól og maurasýru sem og fyrir samkeppnishvarfið að mynda vetnisgas. Til að rannsaka áhrif vatns sem leysis er eitt mónólag af vatnssameindum notað í fríorkureikningum á milliástöndum í CO_2 afoxun og H_2 myndun og borið saman við niðurstöður þegar vatn er ekki til staðar. Við einblínum á hneigð í efnahvötun með hliðsjón af eldfjallamyndum fyrir myndefnin. Við sjáum að vatnsameindirnar sem eru bundnar við yfirborðið geta breytt yfirspennunni í maurasýru og metanól frá 0,2 og upp í 0,5 V en hins vegar breytist ekki hvaða skref er spennutakmarkandi. Niðurstöðurnar gefa til kynna að vatnssameindirnar minnki bindingu HCOOH á yfirborðunum sem hefur mikil áhrif þar sem HCOOH er lykilskref í CO_2 afoxun í metanól. Þá rannsökum við sækni súrefnis-, kolefnis- og vetnisatóma á málmoxíðunum og hlutverk þeirra á virkni og nýtni efnahvatanna. Ítarlegar rannsóknir okkar sýna einnig að CO hula á yfirborði hefur talsverð áhrif á nýtni efnahvatanna í mismunandi myndefni. Fyrir öll málmoxíðin sem eru rannsökuð er meðal há CO hula hagstæð fyrir bæði myndun á maurasýru og á metanóli. Enn fremur er MoO_2 og HfO_2 spáð fyrir um að hvarfa CO_2 í metanól við lága yfirspennu við miðlungs eða háa CO hulu frekar en við lága hulu. Þar að auki benda gögnin til að aukin CO hula á málmoxíðunum geti lækkað vetnismyndunina. Rannsóknirnar undirstrika enn fremur mikilvægi virkra bindistaða á yfirborðinu þegar CO_2 er afoxað í metanól og að nota hentuga vísa af ásogsorku fyrir lykilmilliefni. Þessar niðurstöður eru notaðar í loka verkefni þessarar ritgerðar þar sem við rannsökum virka staði í CO_2 afoxun í CO og maurasýru á TiO_2/RuO_2 og SnO_2/RuO_2 blöndum. Til að skilja niðurstöður tilrauna og spá fyrir um virka hvarfstaði eru Ru atóm skipt út fyrir Ti eða Sn atóm í TiO_2 og SnO_2 með mismunandi hlutföllum og samsetningum. Við sjáum að þegar bindistaðirnir fyrir COOH/OCHO milliefnin eru Ru-Ti er yfirspennan fyrir CO myndun hærri en fyrir RuO_2 yfirborðið, en þegar bindistaðirnir eru Ru-Ru eða Ti-Ti er yfirspennan lægri. Hins vegar fyrir myndun á maurasýru eru Ru-Ru bindistaðir með lægstu yfirspennuna á meðan Ti-Ti bindistaðir eru með hæstu yfirspennuna. Við sjáum einnig að þegar Ru atómi er skipt út fyrir Cu atóm þegar eitt lag af RuO_2 er á TiO_2 yfirborði að yfirspennan lækkar töluvert fyrir bæði myndun á maurasýru og CO. Þá sýna niðurstöður okkar að þegar Sn atómi er skipt út fyrir Ru atóm á ákveðnum stöðum á SnO_2 yfirborðinu að yfirspennan minnkar vegna áhrifa á rafeindabyggingu yfirborðsins. Þessar niðurstöður er hægt að nýta til að hanna virka staði fyrir CO_2 afoxun og þar með hækka nýtni og lækka yfirspennuna sem þarf að leggja á kerfið.

This dissertation is sincerely dedicated to my family and friends

and

the bravest women of Iran fighting for freedom.

#Woman, Life, Freedom.

A special feeling of gratitude to my loving parents who dedicate their lives to me

and,

to my soulmate, Nima, whose words of encouragement and push for tenacity ring in my ears.

Preface

This thesis is submitted in candidacy for a Ph.D. degree from the University of Iceland. The work has been conducted between January 2018 and March 2023 at Faculty of Industrial Engineering, Mechanical Engineering and Computer Sciences supervised by Prof. Egill Skúlason.

Icelandic Research Fund (grant no. 196437-051), the Research Fund of the University of Iceland financially supported the work.

Narges Atrak

March 2023

Table of Contents

List of Figures

List of Tables

List of Papers

I. Atrak, N.; Tayyebi, E.; Skúlason, E., Effect of co-adsorbed water on electrochemical CO_2 reduction reaction on transition metal oxide catalysts, ***Appl. Surf. Sci.***, 2021, 151031.

II. Atrak, N.; Tayyebi, E.; Skúlason, E., Electrochemical CO_2 reduction towards formic acid and methanol on transition metal oxide surfaces as a function of CO coverage, submitted, 2023.

III. Atrak, N.; Tayyebi, E.; Skúlason, E., Insight to active sites for electrocatalytic CO_2(g) reduction to CO(g) and formic acid on RuO_2/TiO_2 and SnO_2/RuO_2 alloys, submitted, 2023.

My contribution to the publications

Paper I

I performed half of the calculations. I did half the analysis of data. I was the main responsible for writing the manuscript.

Paper II

I performed all the calculations and all the analysis of data. I was the main responsible for writing the manuscript.

Paper III

I performed all the calculations and all the analysis of data. I was the main responsible for writing the manuscript.

Abbreviations and symbols

TMO	Transition Metal Oxides
DFT	Density Functional Theory
CHE	Computational Hydrogen Electrode
HER	Hydrogen Evolution Reaction
CO_2RR	Carbon Dioxide Reduction Reaction
SHE	Standard Hydrogen Electrode
U	Applied Potential
ML	Mono Layer
LDA	Local Density Approximation
GGA	Generalized Gradient Approximation
PAW	Projector Augmented Wave
PBE	Perdew-Burke-Eernzerhof
BEEF	Bayesian-Error-Estimation-Functional
RPBE	Revised Perdew-Burke-Eernzerhof
STM	Scanning tunneling microscopy
Ψ	Wave Function
$\hat{H}$	Hamiltonian Operator
E_{xc}	Exchange Correlation Energy
μ	Chemical Potential
ΔG	Free Energy Changes
E_a	Activation Energy
i	Current Density
q^M	Charge on the Metal Electrodes
q^S	Charge in the Solution
σ	Charge Density

C_d	Capacitance
G_{int}	Integral Free Energy
U_{pzc}	Potential of Zero Charge
N	Number of Surface Metal Atoms
n	Number of Protons in Double Layer
atm	Atmosphere pressure

Acknowledgements

I owe a great debt of gratitude to the many individuals in my life for whom the PhD experience was a personally and professionally rewarding adventure. There is no one I would rather have with me on my PhD journey than Dr. Egill to supervise. Having such faith in all of us in the group, he allows us a great deal of independence to develop our minds. I've always admired and tried to emulate his ability to spot patterns in apparently unrelated collections of data and his always constructive comments and ideas. I also want to adopt his method of effective leadership in my future career. Many thanks to Dr. Hannes, who has been a great help in my PhD endeavor. He always inspired me by engaging in many thought-provoking debates and providing me with constructive feedback and also for taking a role as a member of my Ph.D. committee. Special thanks to Dr. Elvar for being a committee member of my Ph.D. dissertation. I have much gratitude for Dr. Ebrahim who has always been not only a mentor but also a great companion over this time. He has always made himself available for my questions and scientific discussions. I benefitted immensely from his extensive knowledge in electrocatalysis.

The lovely people of VRIII deserve particular thanks for being generous with their time with whom I shared good memories. I also thank administrative staff Þuriður and Sandra and Heiður Anna in student housing for always being helpful.

I'd like to extend my gratitude to Dr. Jan Rossmeisl and his group at Copenhagen University for their insightful conversation on the topic of modelling pH and potential in the dynamic structure of the water-solid interface during my academic visit. My appreciation also extends to the people in the Nordic Consortium for CO_2 Conversion, in particular to Dr. Kathrin H. Hopmann the project co-leader of NordCO_2 at University of Tromso, for welcoming me as a member.

I am fortunate to have parents who instilled in me the value of education from a young age, my fiancé who is constantly at my side and my friends who helped to make my time in Iceland the one that I will never forget.

Thanks

Narges Atrak

1 Introduction

1.1 Global warming and causes

Changes in the Earth's climate have been more noticeable since the start of the twentieth century than they were before industrialization, especially in comparison to preindustrial times, as illustrated in Figure 1.1. Fossil fuel (coal, oil, and gas) burning and deforestation are raising carbon dioxide levels in Earth's atmosphere, resulting in an increase in Earth's temperature of around one degree Celsius per decade. (https://climate.nasa.gov/resources/global-warming-vs-climate-change/).

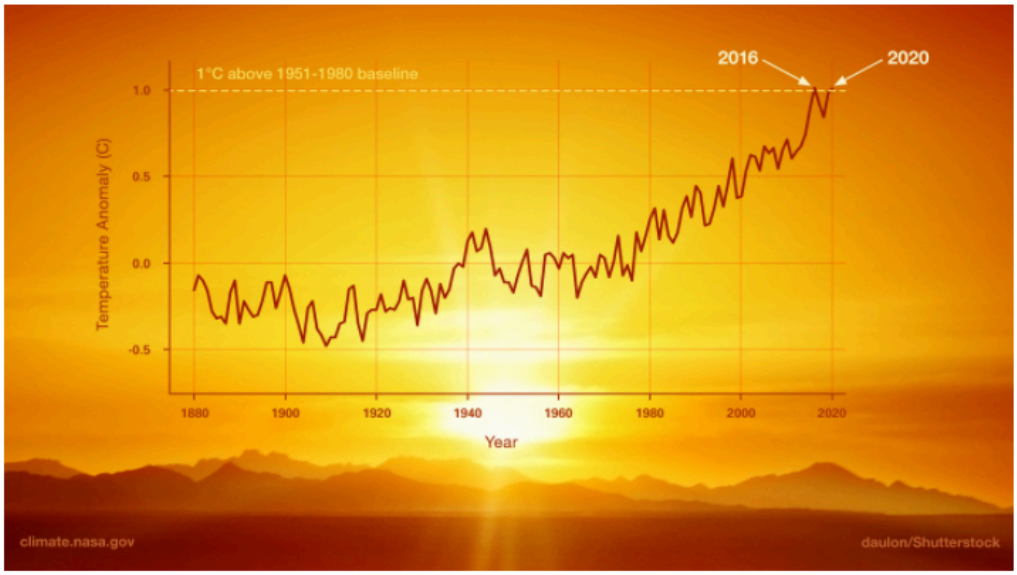

Figure 1.1 Climate data from 1880 to 2020, with the hottest years in that timeframe being 2016 and 2020. Credit: NASA/JPL-Caltech (Source: NASA's Goddard Institute for Space Studies).

Figure 1.2 displays the five-year average change in global warming as captured from the time series on the Nasa webpage. Dark shades of blue denote regions with lower than average temperatures, whereas dark shades of red denote regions with higher than average temperatures.

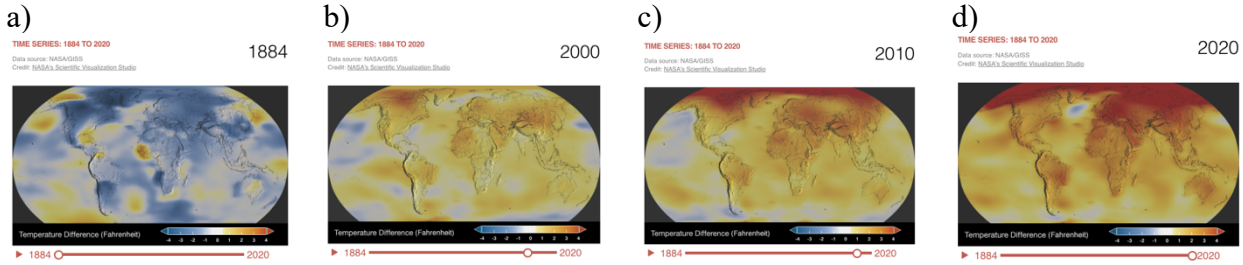

Figure 1.2 Images from Nasa's website illustrate the five-year average global warming change for the years 1884, 2000, 2010, and 2020, respectively. (Source: climate.nasa.gov)

The most significant greenhouse gas is carbon dioxide, which causes the surface temperature to rise by absorbing the Earth's surface's emission of infrared radiation and retaining the heat there. Scientists believe that the unprecedented increase in the temperature of the Earth and, as a result, the rise in sea levels, the loss of glaciers, and severe changes in weather conditions such as heatwaves, hurricanes, floods, etc., and so many more to name are providing evidence of an impending disaster[1] (https://climate.nasa.gov/resources/global-warming-vs-climate-change/). According to the Intergovernmental Panel on Climate Change (IPCC) report (https://www.ipcc.ch/2021/08/09/ar6-wg1-20210809-pr/), new estimates reveal that the global warming level may reach or even exceed 1.5°C in the next decades in roughly over the next 20 years and that limiting the warming will be nearly impossible unless immediate actions are taken to reduce greenhouse gas emissions.

Figure 1.3 As temperatures rise in the future, California will continue to suffer from a long-term drought. Credit: Robyn Beck/AFP/Getty (Source: https://www.nature.com/articles/d41586-021-02179-1)

Decreasing greenhouse gases and carbon dioxide emissions could help to tackle climate change and global warming, which according to the IPCC Working Group I report might take 20-30 years to stabilize Earth's temperature (IPCC Working Group I report, Climate Change 2021: the Physical Science Basis, approved on Friday by 195 member governments of the IPCC). "Stabilizing the climate will require strong, rapid, and sustained reductions in greenhouse gas emissions, and reaching net zero CO_2 emissions. Limiting other greenhouse gases and air pollutants, especially methane, could have benefits both for health and the climate," said Zhai, IPCC Working Group I Co-Chair (https://www.ipcc.ch/2021/08/09/ar6-wg1-20210809-pr/).

Figure 1.4 Heavy rainfall and flood in Zhengzhou, Henan province, China, in July 2021 because of climate change. Credit: Aly Song/Reuters/Alamy. (Source: https://www.nature.com/articles/d41586-021-02150-0)

According to satellite data taken by NASA and displayed in Figure 1.5, global warming is causing a considerable decrease in the arctic sea ice extent over the entire year. Accordingly, the rate of change is 13.0 percent per decade, with the year 2012 sea ice extent reported to be the lowest in the satellite record. The melting of ice sheets and glaciers is contributing to an overall rise in sea level. The most recent measurement of the sea level, which took place in July 2021, was 99 (±4.0) millimeters, according to the data collected from the satellites, and the rate of change was estimated to be 3.4 millimeters per year.

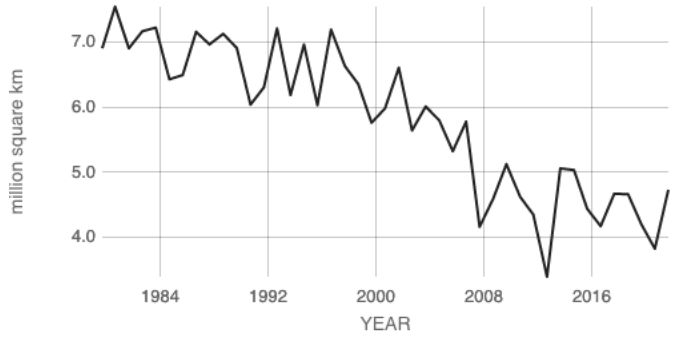

Figure 1.5 Arctic Sea ice extent in all months recorded by satellite. (Source: climate.nasa.gov)

The rise in the internal temperature of ocean water as a result of global warming is another recognized driver of global sea level rise. This gain in temperature causes glaciers to melt, which in turn causes water to expand. The year 2020 known as the warmest year, has the highest record in sea level rise. The majority of the surface of the Earth is covered by seas, and rising concentrations of greenhouse gases are responsible for the warming of the oceans, particularly in the upper few meters where a lot of heat is retained. This has a direct impact on the rising of sea levels as well as the health of marine life and the biochemistry of the ocean.

1.2 Carbon dioxide

Carbon dioxide (CO_2) is an odorless and colorless greenhouse gas that makes up a negligible portion of the atmosphere of Earth. Deforestation, the combustion of fossil fuels, volcanic eruptions, and other natural processes all contribute to the production of carbon dioxide (CO_2), which is recognized to be the primary agent behind climate change. The levels of carbon dioxide, measured in parts per million (ppm), have been steadily increasing over the years, as seen in Figure 1.6.

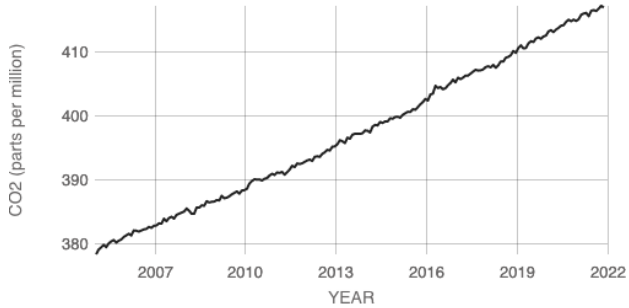

Figure 1.6 Monthly observations of CO_2 concentrations in parts per million (ppm) taken at the Mauna Loa Observatory in Hawaii during the past few years. (Source: climate.nasa.gov)

In another graph created by NASA, titled Figure 1.7, it is shown that CO_2 concentrations have increased by approximately 49 percent since the pre-industrial era. This increase is remarkable when compared to the naturally occurring increase in CO_2 concentrations that happened from the period of the Last Glacial Maximum to 1850, which ranged from 185 ppm to 280 ppm.

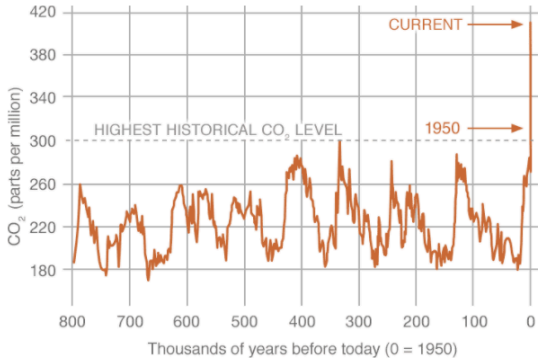

Figure 1.7 The concentration of carbon dioxide, measured in parts per million (ppm), during each of the three most recent glacial cycles, as reconstructed from ice cores. (Source: climate.nasa.gov)

The variation in CO_2 concentrations that occurred over the course of the years from 2002 to 2016 is also depicted in snapshots from a time series that are published on the NASA website once every five years. As time passes, the concentration of CO_2 in the atmosphere continues to rise, causing the hue of the map to become increasingly red.

a) b) c) d)

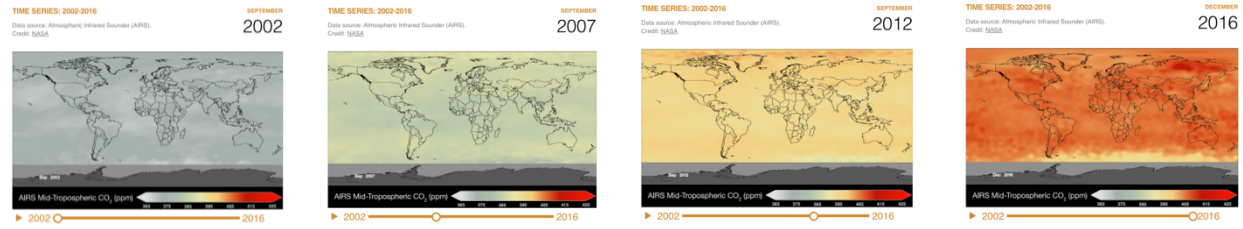

Figure 1.8 pictures taken from a time series published on the NASA website for the years 2002, 2007, 2012, and 2016 respectively. (Source: climate.nasa.gov)

Human-induced carbon has a long lifetime in the atmosphere and half of it could be removed by the natural carbon cycle in a century. However, a considerable amount of emitted CO_2 remains in the atmosphere for thousands of years[2]. According to Montenegro et al.[3] recent analysis, only a quarter of CO_2 emissions has a long lifetime of more than five millennia. Therefore, by decreasing the atmospheric CO_2, global temperatures will decrease in response[4].

1.3 Beyond Fossil fuels and alternative energy sources

It is well recognized that coal, oil, and natural gas are the primary fossil fuels that serve not only as our primary sources of energy but also as feedstocks for a wide variety of materials

and chemicals. On the other hand, the sources of fossil fuel, which have been developed over the period of eons, are fast getting depleted as a result of the ever-increasing energy demand of civilization. The ongoing depletion of fossil fuels will cause their prices to rise, necessitating the search for alternative sources of energy as well as potential remedies[5]. Taking into account all of the potential alternative energy sources, such as hydrothermal and geothermal energies, seems to be a satisfactory response to the ever-increasing energy demands of civilization. The utilization of those energies, on the other hand, as a replacement for fossil fuels in order to fulfil the requirements of a growing global population is not likely to have a substantial impact on the energy forecast for the future (Energy Technologies for the 21st Century, International Energy Agency, Paris, 1997). Other forms of alternative energy, such as nuclear power and hydrogen gas, each have their own set of advantages and disadvantages. Since nuclear energy was first utilized as an atomic weapon against mankind during World War II, public opinion has always been dubious regarding the use of nuclear energy for any reason, even peaceful purposes. Hydrogen, on the other hand, is not a renewable resource here on Earth due to its lack of compatibility with the high oxygen concentration of our atmosphere. Aside from being exceedingly energy intensive, the production of hydrogen is not necessarily a green activity. Hydrogen may be generated either by electrolysis of water or through the reformation of fossil fuels to produce synthetic gas, a combination of CO and H_2. For this reason, great precautions must be taken when storing or transporting hydrogen gas because even the smallest leak might result in an explosive event.

Owing to the serious limitations of mentioned energy sources, methanol, seems a relatively convenient alternative for fossil fuels[6–9]. Methanol is an easily stored chemical that may be produced by either the direct oxidative conversion of natural gas (methane) or the reductive conversion of carbon dioxide with hydrogen. Both of these processes are possible. It is also capable of being combined with gasoline and possesses a reasonably high energy density. As a result, it may serve both as a practical fuel and as a raw material for the production of man-made hydrocarbons and the goods derived from them.

Converting CO_2 to hydrocarbon-based products with a renewable energy source is not only a solution to reduce hazardous CO_2 emissions and consequently, tackle global warming, but also to gradually replace fossil fuels with renewable carbon-based fuels such as methanol[10]. In this regard, electrochemical CO_2 reduction reaction (CO_2RR) is known to be one of the most promising approaches for storing renewable electricity as chemical energy in fuels[11]. In the next section, we will discuss more about CO_2RR.

1.4 Electrochemical conversion of carbon dioxide (CO_2) to fuel

As mentioned earlier, one of the promising approaches to decrease CO_2 emissions is to use CO_2 as a reactant and a renewable energy source (such as geothermal, wind or solar energy) to convert it to particular hydrocarbons (HCAs) as synthetic fuels or other carbon-based products as abovementioned. Carbon Recycling International (CRI) plant, which is operating in Iceland, is the globally recognized leader in converting CO_2 to methanol technology (https://www.carbonrecycling.is). At CRI, commercial production of renewable methanol begins with the electrolysis of water to generate hydrogen, which is then followed by the reaction of the hydrogen with carbon dioxide. They believe that their latest plant under

construction will be the largest of its type in the world, with the ability of recycling approximately160,000 tons per year of CO_2 into methanol (https://www.carbonrecycling.is).

The electrochemical CO_2RR process is difficult to drive, and there are a lot of parameters that need to be addressed. One of these is the design of the catalyst in such a way that it can carry out the CO_2 reduction reaction at very low overpotentials while maintaining a high selectivity toward particular hydrocarbons rather than byproducts such as hydrogen evolution. This is the most important of the design considerations, and yet one of the most challenging. Among the single metallic systems studied primitively, copper (Cu) is the only metallic catalyst shown to be the most efficient in reducing CO_2 to hydrocarbons and oxygenates such as methane, ethylene and ethanol, whereas other metals produce only hydrogen, formate or CO[12–14]. Cu, on the other hand, is not selective because it results in the production of a mixture of hydrocarbons and alcohols in CO_2RR and because it requires an overpotential of 1VRHE to reduce CO_2. These factors have prohibited practical applications of Cu for the aim of efficient energy conversion[15–17]. Additionally, methanol has only been produced in trace amounts (below 0.1% for all metals except Ni where it is around 3% in current efficiency, CE) in CO_2RR explored on all metallic catalysts[18]. All potentials reported throughout this dissertation are with respect to RHE, and for the remainder of the article the RHE notation is dropped.

The search for a catalyst for CO_2RR that is both highly efficient and adequately selective has led researchers to a distinct family of materials known as transition metal dioxides (TMOs), which have been reported to be active at significantly lower overpotentials ranging from ~0.1 to ~0.3 V[19–23]. TMOs, in contrast to metals, which bind the corresponding intermediates through their carbon atom, are predicted to bind all CO_2RR intermediates through their oxygen atom(s), according to DFT studies carried out in our group. The oxygen vacancy that exists in bridge sites on TMO surfaces is the reason for this prediction[24]. Therefore, the oxygen atom(s) bound to the TMO surfaces are less likely to be protonated and rather carbon atom is reduced resulting in higher efficiency toward formic acid and/or methanol formation than e.g., methane. While on metal surfaces, the oxygen atom(s) point away from the surface being exposed to the electrolyte solution and hens a high efficiency of methane is observed.

Extensive experimental studies were conducted for CO_2RR[19–23,25], HER[26] and oxygen evolution reaction (OER)[27] on RuO_x-based catalysts. Accordingly, RuO_2-based catalysts can reduce CO_2 to methanol at low overpotentials with high selectivity. Some factors, such as catalyst composition and reaction conditions, affected the products and their efficiencies during these studies. Up to 24% faradic efficiency for methanol and 78% for formic acid was obtained with RuO_2/TiO_2 alloy electrocatalyst at ~-0.15V and pH=1.2 in 0.05 M H_2SO_4 electrolyte. But 76% faradic efficiency for methanol was obtained with the same electrocatalyst by setting the potential near "water reduction potential" and the pH=4 in 0.2 M Na_2SO_4 electrolyte[19]. Adding Cu species on the surface of the alloy electrocatalyst slightly improved the faradic efficiency for methanol to 29.8% but for formic acid dropped to 4.2% at ~0.15V at pH =7.2–7.3 in 0.5 M $KHCO_3$ electrolyte[20]. In addition, Cd and Cu modified RuO_2 electrodes show faradic efficiency of 38.2% and 41.3% toward methanol at ~-0.15V in 0.5 M $NaHCO_3$ electrolyte, respectively[23]. A faradic efficiency of 60.5% for methanol with RuO_2 nanoparticles on TiO_2 nanotubes substrate at ~-0.15 V has also been reported[22]. Moreover, up to 60.5% faradic efficiency for methanol was achieved with RuO_2 particles deposited on TiO_2 substrate, whereas by changing the substrate to boron-doped diamond

faradic efficiency for methanol has dropped to 8.1% and a faradic efficiency of 32.66% for formic acid was obtained[21].

In contrast to previous experimental studies where methanol and/or formic acid have been observed to be the major products, hydrogen gas has been reported to be the dominant product according to an experimental work on RuO_2[25]. In addition, some trace amounts of formate and CO(g) were detected in their experiment and the corresponding efficiencies are reported to increase when mixing RuO_2 with Ti and Sn, and also doping it with Cu[25]. They have tried to redo almost all the previous experimental works[19–23] but they have not succeeded in detecting any methanol as a product under any experimental conditions. However, they illustrated that RuO_2 could bind both CO and CO_2 on the surface although it is not an active catalyst for electrocatalytic conversion of CO_2 to methanol.

DFT based calculations have been employed to study CO_2RR toward methanol, formic acid, methanediol and methane on RuO_2-based catalysts using the rutile crystal structure and (110) facet as a model system. In these studies, the mechanism and reaction pathway for CO_2RR has been proposed[28]. Additionally, the effect of different transition metal oxide overlayers such as Ir, Mo, Nb, Pd, Pt, Re, Sn, Ta, Ti, and W on top of RuO_2 and also the mixture of $Ir_xRu_{(1-x)}O_2$ has been studied[29]. Follow up works have further broadened our understanding of CO_2RR by expanding the studies to catalysts other than RuO_2 such as IrO_2, NbO_2, PtO_2, TiO_2, CrO_2, MnO_2, RhO_2, OsO_2, HfO_2, MoO_2, and PdO_2[30]. The thermochemical model and computational hydrogen electrode (TCM-CHE)[31] approach has been used to carry out all these studies, which will be discussed in detail in next chapter.

These results seem promising than metallic catalysts for methanol or formic acid evolution in CO_2RR. Such an exceptional behavior of oxide catalysts compared to metallic ones for converting CO_2 to fuels indicates possible different reaction mechanisms or disparate scaling laws governing the reactions.

1.5 Computational catalyst design

Computational materials science is a bridge that connects experiments and theory. In order to study the physical phenomenon, computational materials science uses different physical and chemical models. Therefore, for a better representation of an actual physical phenomenon, a less approximate model is required. Thus, simulation-based materials design is becoming more reliable. In some part of our work, we have included the presence of water in order to have a more accurate model system.

Due to its versatility, water plays a critical role in a wide variety of chemical processes. Because of the abundance of chemistry it contains, water is an essential component in a broad range of chemical and biological processes; in fact, several of these reactions cannot occur without the presence of water. In the surroundings of a chemical reaction, a water molecule may appear as an individual molecule, or it may adsorb onto the surface in dissociated or undissociated forms, depending on the system. In addition, it may exhibit an inert behavior in some circumstances, but it may also rapidly oxidize the surface in the form of an adsorbed molecule on the surface. Despite the fact that the cooperative adsorption of water molecules in reactions, also known as co-adsorption, can have an effect on the configurations and binding strengths of other adjacent adsorbates on the surface, this

molecule also takes part in a great number of electrocatalytic reactions, such as the CO_2RR[32–34]. In electrocatalytic processes, which are carried out in aqueous solutions, it has been well established that the presence of water can have an effect on the binding strength, configurations, and stability of adsorbates on the surface. Therefore, it is vital to also take into consideration the solvation influence that this molecule has on the reactants, intermediates, and products in the reaction. Because it has been shown that utilizing density functional theory (DFT) computations to simulate solid-liquid interfaces may be fairly challenging, it is vital to have functionals that are efficient in order to be able to characterize the hydrogen bonding interactions[35–38]. CO_2RR is an example in which rational design of a new class of catalysts with high selectivity and efficiency toward specific hydrocarbons or oxygenates (e.g., alcohols) is important and the presence of water may massively alter the results[39]. Recently an electrochemical solid-liquid interface model has been able to successfully predict the experimental product distribution of CO_2RR on metals as a function of applied potential[24]. However, no realistic model system has been developed for transition metal oxides (TMOs), which could be due to the lack of a better understanding of molecular structure of water on TMOs than metals. The thermochemical model (TCM) and computational hydrogen electrode (CHE), on the other hand, has aided to capture the overpotentials for CO_2RR and other electrochemical reactions on metal oxides quite well, though they are unable to capture experimental trends[40–44]. It has been established that water molecules bind physically on metal surfaces whereas on TMOs they bind chemically via oxygen atoms on coordinately unsaturated site (CUS)[24,33,37,45–49]. An experimental study using high resolution electron energy loss spectroscopy (HREELS) and thermal desorption spectroscopy (TDS) carried out on $RuO_2(110)$ surface also confirmed the binding of water molecules via oxygen atoms on CUS[33]. Accordingly, water dissociation was not observed to occur on CUS, while it occurs on some vacant bridge sites in small amount.

This thesis explores avenues of understanding instinctive features of CO_2RR on different TMOs, factors governing activity and propose guidelines for a rational design of an electrocatalyst for an efficient electrochemical conversion of CO_2 to fuel.

1.6 Thesis outline

In this dissertation, we employ the TCM-CHE method to examine the effect of solvent (co-adsorbed water) on the binding energy of CO_2RR intermediates, the constructed activity and selectivity volcano-plots for formic acid and methanol, and the estimated overpotentials. Next, the surface CO coverage as an important parameter for predicting selectivity trends in electrochemical CO_2 reduction reaction has been investigated intensively. Last but not least, we investigated CO_2RR on RuO_2-based catalysts such as alloys of TiO_2:RuO_2 and SnO_2:RuO_2 s using the instructions and guidelines obtained thus far.

2 Introduction to theoretical background

Physicists, chemists, material scientists, and engineers across disciplines are increasingly turning to density functional theory (DFT) based computations to solve diverse materials modelling problems. DFT is a remarkably effective method for finding solutions to the fundamental Schrödinger equation[50] that defines the quantum behaviour of atoms and molecules in contexts of practical importance[51,52]. This chapter focuses on the requirements for performing well-converged DFT computations. After all, before we can debate the agreement (or lack thereof) between DFT results and physical reality, we need to be able to reliably identify accurate solutions to the numerical issues given by DFT.

2.1 The Schrödinger equation

One of the essential things to know about atoms and molecules is their energy and, more significantly, how their energy varies when they move around. In other words, using quantum mechanics, atoms and molecules can be described in terms of interactions between electrons and nuclei. The Schrödinger equation[50] underlies all quantum mechanical approaches, which can be solved perfectly for the hydrogen atom as illustrated in equation (1).

$$\left[-\frac{1}{2}\nabla^2 - \frac{Z}{r}\right]\psi(r) = E\psi(r) \quad (1)$$

Where r is the electron distance from a nucleus of charge Z, E is the ground state electronic energy and ψ is a wavefunction defining the electron movement. The value in square brackets indicates the kinetic and potential energies of an electron.

The generalized time-independent, nonrelativistic Schrödinger equation is $H\psi = E\psi$ where H is the Hamiltonian operator and ψ is the eigenstates of the Hamiltonian or many-electron wavefunction. This form of Schrödinger equation is the simple form of it but it is more complicated in the case of multiple electrons interacting with multiple nuclei, which can be expressed as follows:

$$\left[\frac{h^2}{2m}\sum_{i=1}^{N}\nabla_i^2 + \sum_{i=1}^{N}V(r_i) + \sum_{i=1}^{N}\sum_{j>i}U(r_i, r_j)\right]\psi = E\psi \quad (2)$$

Here, *m* is the electron mass and *h* is the Plank´s constant. The three terms in brackets define the kinetic energy of each electron, the interaction energy between each electron and the nuclei, and the interaction energy between electrons, respectively. ψ is a function of the spatial coordinates of each N electrons. The Hamiltonian can be given in atomic units as follows:

$$H = -\frac{1}{2}\sum_{i}^{electrons}\nabla_i^2 - \frac{1}{2}\sum_{A}^{nuclei}\frac{1}{M_A}\nabla_A^2 - \sum_{i}^{electrons}\sum_{A}^{nuclei}\frac{Z_A}{r_{iA}} + \sum_{j>i}^{electrons}\sum\frac{1}{r_{ij}} + \sum_{B>A}^{nuclei}\sum\frac{Z_A Z_B}{R_{AB}} \quad (3)$$

Here, M_A is the mass of nucleus A, Z is the nuclear charge, r_{iA} is the distance between electron i and nucleus A, r_{ij} is the distance between electrons i and j, and R_{AB} is the distance between nuclei A and B.

The Schrödinger equation is a many-body problem. Even for a basic two-electron system like a helium atom or hydrogen molecule, the many-electron Schrödinger equation cannot be solved correctly. In order to create workable solutions, approximations must be established.

2.2 Born-Oppenheimer Approximation

To determine the location of an atom, it is necessary to define the location of both its nucleus and electrons. An important fact in applying quantum mechanics to atoms is that atomic nuclei are significantly heavier than individual electrons such that each proton or neutron in a nucleus has a mass that is more than 1,800 times that of an electron implying that electrons respond to changes in their surroundings far more quickly than nuclei. As a result, the Schrödinger equation can be simplified, splitted into two parts: electron motion and nuclear motion. The division of the nuclei and electrons‘ motion into independent mathematical problems is the Born-Oppenheimer approximation[53]. If there are M nuclei at R_1,..., R_M locations, the ground-state energy can be indicated as a function of the locations of these nuclei, E(R_1,..., R_M). By calculating the potential energy surface, the question regarding how the energy of the material changes as its atoms move around would be tackled.

By doing so, the Born-Oppenheimer approximation leads to an electronic Schrödinger equation where the electronic Hamiltonian (H^{el}) will be as follows:

$$H^{el} = -\frac{1}{2}\sum_i^{electrons}\nabla_i^2 - \sum_i^{electrons}\sum_A^{nuclei}\frac{Z_A}{r_{iA}} + \sum_{j>i}^{electrons}\sum\frac{1}{r_{ij}} \quad (4)$$

In this equation, the term expressing nuclear kinetic energy is absent (equal to zero), and the nuclear-nuclear Coulomb value is a constant. To get the total energy for the system, the latter must be added to the electronic energy, E^{el}.

$$E = E^{el} + \sum_{B>A}^{nuclei}\sum\frac{Z_A Z_B}{R_{AB}} \quad (5)$$

2.3 The advent of density functional theory

As explained in the previous section, practically solving a Schrödinger equation enatils solving a many-body problem. As in terms of solving the equation, the component in the Hamiltonian characterising electron–electron interactions is the most crucial and $\psi_i(r)$ cannot be determined without considering individual electron wave functions simultaneously associated with all other electrons. It is not possible to directly view the wave function for any given set of coordinates. Moreover, it should be noted that electrons cannot practically be labled. The quantity that can be measured is the chance that N electrons are located at a specific set of coordinates or in other words the density of electrons at a particular position in space. This may be expressed in terms of the individual wave functions of electrons:

$$n(r) = 2 \sum_i \psi_i^*(r)\psi_i(r) \quad (6)$$

Here, the summing includes all electron-occupied individual wave functions, therefore the term inside the summation represents the probability that an electron in individual wave function $\psi_i(r)$ is positioned at r. The aim is to find the ground-state energy of the Schrödinger equation, but it is extremely difficult as it is a many-body problem.

In the mid-1960s, Kohn and Sham[54] derived a series of equations based on two fundamental mathematical theorems established by Kohn and Hohenberg[55–58]. According to Hohenberg and Kohn theorem, there is a one-to-one mapping between the ground state wave function and the ground state electron density. Another approach to express Hohenberg and Kohn's conclusion is to say that the ground-state electron density influences all features of the ground state, including the energy and wave function. This result is important as the Schrödinger equation is possible to be conceived by finding a function of three spatial variables (the electron density) rather than the wave function, which is a function of 3N spatial variables. While the first Hohenberg–Kohn theorem establishes that a functional of electron density exists that may be utilised to solve the Schrödinger equation, it does not explain what this functional is. A crucial property of the functional, as defined by the second Hohenberg–Kohn theorem, is the fact that full solution of the Schrödinger equation is the genuine electron density, which may be found by finding the lowest energy of the overall functional. The Hohenberg-Kohn theorem's functional may be expressed in terms of the wave functions of single electrons i.e. $\psi_i(r)$. The energy functional may be expressed as follows:

$$E[\{\psi_i\}] = E_{known}[\{\psi_i\}] + E_{XC}[\{\psi_i\}] \quad (7)$$

Where the functional can be splitted into a collection of terms expressed in a simple analytical form, $E_{known}[\{\psi_i\}]$, and E_{XC} is the exchange–correlation functional, and is defined to include all the quantum mechanical effects that are not included in the “known” term. Contributions to the "known" term include the following:

$$E_{known}[\{\psi_i\}] = \frac{h^2}{m} \sum_i \int \psi_i^* \nabla^2 \psi_i d^3r + \int V(r)n(r)\, d^3r + \frac{e^2}{2} \int \int \frac{n(r)n(r')}{|r-r'|} d^3r\, d^3r' + E_{ion} \quad (8)$$

Where the terms on the right part of the equation are the electron kinetic energies, the Coulomb interactions between the electrons and the nuclei, the Coulomb interactions between pairs of electrons, and the Coulomb interactions between pairs of nuclei, respectively. The Hohenberg-Kohn theorem merely establishes that the energy is a functional of density, however, it does not specify how to achieve this functional. In 1965, Kohn and Sham proposed a scheme for approximatively determining the functional. Kohn and Sham demonstrated that finding the proper electron density may be described as a series of equations in which each equation only deals with a single electron. The Kohn–Sham equations are expressed as follows:

$$\left[\frac{h^2}{2m} \nabla^2 + V(r) + V_H(r) + V_{XC}(r)\right] \psi_i(r) = \varepsilon_i \psi_i(r) \quad (9)$$

Where $V(r)$ potential defines the interaction between an electron and the atomic nuclei and $V_H(r)$ is the Hartree potential which describes the Coulomb repulsion between one electron and the total electron density and is defined as follows:

$$V_H(r) = e^2 \int \frac{n(r')}{|r - r'|} d^3r' \quad (10)$$

As the electron in the Kohn–Sham equation is also a component of the overall electron density, a Coulomb interaction between the electron and itself is included in the Hartree potential as a self-interaction contribution. $V_{XC}(r)$ characterise exchange and correlation contributions to single electron equations and include the correction for the self-interaction effect. $V_{XC}(r)$ can be described as follows:

$$V_{XC}(r) = \frac{\delta E_{XC}(r)}{\delta n(r)} \quad (11)$$

The equation (9) is similar to equation (2) except that the Kohn–Sham equations are missing the summations, which is because the solution of the Kohn–Sham equations are single-electron wave functions that depend on only three spatial variables.

There is a vague sense of some cycle existing about the Kohn–Sham equations such that in order to solve the Kohn-Sham equations, the Hartree potential must be defined, and the electron density must be known in order to determine the Hartree potential. But the single-electron wave functions must be known to discover the electron density, and to solve the Kohn–Sham equations to these wave functions must be known. To break this cycle, the problem is frequently approached iteratively in a way that, firstly an initial, trial electron density can be defined. Secondly, the Kohn–Shame quations defined using the trial electron density can be solved and then the electron density defined by the Kohn–Sham single particle wave functions can be solved. Next, the calculated electron density with the electron density used in solving the Kohn–Sham equations can be compared. After the comparison, if the two densities are the same, it implies that the ground state electron density has been found and it can be used further to calculate the total energy. If the two densities vary, the trial electron density must be revised. This is an iterative method leading to a solution to the Kohn–Sham equations, which is self-consistent.

2.4 Exchange–correlation functional

Kohn, Hohenberg, and Sham's stunning findings demonstrated that the ground state may be achieved by minimising the energy of an energy functional, which can be accomplished by finding a self-consistent solution to a set of single-particle equations. The only issue is that the exchange–correlation function must be defined to solve the Kohn–Sham equations, which seems very difficult. Indeed, the real form of the exchange–correlation functional remains unknown. Luckily, the uniform electron gas is one example in which this functional can be precisely determined. In this case, there is a uniform distribution of the electron density throughout the space meaning that the electron density is constant at all points. To do so, each position's exchange–correlation potential is set to be equal to the known exchange–correlation potential from a uniform gas at the electron density measured there:

$$V_{XC}(r) = V_{XC}^{electron\ gas}[n(r)] \quad (12)$$

The approximation is named local density approximation (LDA)[59] because it only employs the local density to build the approximate exchange–correlation functional. Employing the LDA, the Kohn-Sham equations can be fully described, but it's important to realise that since

we are not utilising the genuine exchange–correlation functional, the results don't exactly solve the true Schrödinger equation. To this day, many quantum chemistry researchers are focused on developing functionals that are more accurate representations of nature. Over the years a number of approximation functionals have been extensively employed and have been shown to produce satisfactory outcomes solving a wide range of physical issues. The most well-known class of functional after the LDA, which employs the local electron density and local gradient in the electron density is the generalised gradient approximation (GGA)[60] and includes more physical information than the LDA. There are a range of distinct GGA functionals developed due to the flexibility with which gradient-based electron density information may be included. The Perdew–Burke–Ernzerhof functional (PBE)[61,62] and Bayesian Error Estimation Functional (BEEF)[63] are of the most commonly employed functionals in computations involving solids with good accuracy in atomistic catalysis process simulation. BEEF functional as well as vdW-DF2 nonlocal correlation energy and potential function have been utilized throughout this work.

2.5 Reciprocal space and k points

Periodic solids in three dimensions were among the first systems for which the theory of electronic structure was developed. The notion of an electronic band structure dates back to the first decade after the development of quantum physics, with early examples appearing in the works of Sommerfeld and Bethe[64], Slater[65], and others. The total energy of the electrons and nuclei in an elementary unit cell of a crystalline solid has been the subject of theoretical study for over fifty years[66]. The initial venture into the domain of numerical convergence leads out of the familiar three-dimensional physical space where atom locations are established and into what is known as reciprocal space (or k-space, as it is often known). Reciprocal space and its principles are crucial to much of solid-state physics. In a way that, summation over the reciprocal space is necessary to achieve the total energy of the electrons and nuclei in a primary unit cell. Consequently, a number of articles concerning the sampling of k-space were published during the 1970s[67–71]. Choosing the most optimal set of special k-points was the primary focus of these early efforts since computer resources were more constrained back then. Computing power increasing has allowed computational physicists and materials scientists to tackle more complicated systems with hundreds of atoms per unit cell.

2.5.1 Plane Waves and the Brillouin Zone

The solution to Schrödinger equation for a periodic system must satisfy Bloch's theorem, stating that the solution can be expressed as a sum of terms as illustrated in equation (13):

$$\phi_k(r) = \exp(ik \cdot r) u_k(r) \quad (13)$$

Where $u_k(r)$ is periodic in space and is $u_k(r) = u_k(r + n_1 a_1 + n_2 a_2 + n_3 a_3)$ for any integers n_1, n_2 and n_3 and $\exp(ik \cdot r)$ are plane waves. The Schrödinger equation may be solved separately for each value of k, according to this theorem. Many elements of the mathematical issues offered by DFT turn out to be far easier to address in terms of k than in terms of r. Reciprocal space, or simply k space, is the space where k vectors exist. The positions in reciprocal space are defined in terms of the reciprocal lattice vectors and can be defined as follows:

$$b_1 = 2\pi \frac{a_2 \times a_3}{a_1 \cdot (a_2 \times a_3)} \quad (14)$$

$$b_2 = 2\pi \frac{a_3 \times a_1}{a_2 \cdot (a_{13} \times a_1)} \quad (15)$$

$$b_3 = 2\pi \frac{a_1 \times a_2}{a_3 \cdot (a_1 \times a_2)} \quad (16)$$

Where a_1, a_2 and a_3 are the lattice vectors in real space stating that the larger vectors in real space can be converted to smaller vectors in reciprocal space. In this regard the calculations will be simplified and less expensive, which highliths the importanec of conveying the calculations in reciprocal space.

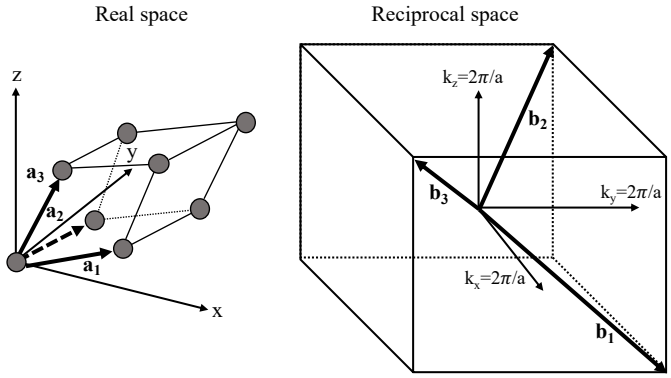

Figure 2.1 Schematic view of the real space and reciprocal space lattice vectors for the fcc primitive cell. the circles in real space represent atoms. The basis vectors in reciprocal space are shown inside a cube.

In Figure 2.1, real and reciprocal views of these lattice vectors are displayed. In simpler terms, a primitive cell can be defined in reciprocal space called Brillouin zone (BZ). There are several points in BZ with different names among which the most important one is Γ point where $k = 0$ and is the origin in reciprocal space. The volume of the BZ can be obtained using the volume of the primitive cell in real space (V_{cell}) defined by the Wigner–Seitz construction.

$$V_{BZ} = \frac{(2\pi)^3}{V_{cell}} \quad (17)$$

2.5.2 Integrals in k Space

A large portion of the effort in a practical DFT computation consists of solving integrals of the form equation (18):

$$g = \frac{V_{cell}}{(2\pi)^3} \int_{BZ} g(k) dk \quad (18)$$

The main characteristics of this integral are that it is specified in reciprocal space and that it only integrates over the Brillouin zone's possible k values.

2.5.3 Choosing k Points in the Brillouin Zone

To do calculations for real-space unit cells containing a large number of atoms, early computational effort centred on the selection of k- points for Brillouin zone sampling that was economically viable. The value of the integrand at a specific place, the so-called Baldereschi[68] point, may be used to approximate the Brillouin zone integral in a rough manner. For more exact calculations, however, a larger number of special k-points is required. One of the approaches in choosing convenient k points is with accordance to Monkhorst-Pack grid which was developed in 1976 by Monkhorst and Pack[71]. This approach of selecting k points is available in the majority of DFT packages. To employ this method, it is sufficient to define the number of k points to be utilised in each direction in reciprocal space. When M k points are utilised in each direction, the computations are usually labelled as M × M × M k points. Using higher k values will lead to more accurate results as the obtained energy will be more precise. In other words, a sufficient number of k points will give a well-converged result which means inevitably using more computational time. It should be noted that using even values of M, a slightly better convergence can be expected than with odd values of M. Of course, having well converged calculations in terms of k points is always preferable, and regrding the distinction between even and odd k-point values is not as important[58].

2.5.4 Smearing method

The Brillouin zone in a metal can be separated into electron-occupied and unoccupied parts. The boundary between these two areas in k space is the Fermi surface. When integrating in k-space, this introduces a considerable complexity because near the Fermi surface, the integrated functions discontinuously transition from nonzero to zero. It takes a lot of k points to produce accurate answers if no additional effort is put into computing these integrals. To overcome this issue, so many useful algorithms have been developed to improve their slow convergence. In this respect, one of the well-known methods is tetrahedron method. The idea is to build a collection of tetrahedra that fill reciprocal space using a discrete set of k points and then use interpolation to specify the function being integrated at each point in a tetrahedron. The function that has to be integrated will have a simple form at all places in k space once this interpolation has been finished, and the integral will be evaluated using the entire space rather than just the discrete points it was initially based on.

The other approach are smearing methods which offer a novel way to address the discontinuous integrals for metals. The objective behind employing a smearing approach to evaluate integrals is to substitute any step functions with smooth functions like the Fermi–Dirac function, which is a continuous function that can be integrated with traditional methods. The calculation's result should ideally be determined using a method that extrapolates the final result to the point that smearing is removed. Methfessel and Paxton are credited with developing a method of smearing that has now gained widespread use.

2.5.5 Energy cutoffs

As mentioned earlier, the solution to the Schrödinger equation should be as equation (13) according to Bloch's theorem. There, due to the periodic nature of $u_k(r)$, it is possible to express it as an expansion in terms of a unique set of plane waves as illustrated in equation (19):

$$u_k(r) = \sum_G c_G \, exp[iG \cdot r] \quad (19)$$

where the summations overall vectors $G = m_1 b_1 + m_2 b_2 + m_3 b_3$ in reciprocal space with integer values for m_i. implementing equation (19) and equation (13) gives equation (20):

$$\phi_k(r) = \sum_G c_{k+G} \, exp[i(k+G)r] \quad (20)$$

According to this equation, a summation over an unlimited number of possible values of G is required to evaluate the answer at even a single point in k space which sounds complicated to solve. However, there are solutions with kinetic energy simplifying the solutions to this equation and have the form:

$$E = \frac{h^2}{2m} |k+G|^2 \quad (21)$$

Physically, lower energy solutions are more significant than higher energy ones. So, it is common that the infinite sum above is truncated to only consider solutions with kinetic energy lower than a certain threshold:

$$E_{cut} = \frac{h^2}{2m} G_{cut}^2 \quad (22)$$

Where E_{cut} is the cutoff energy. In other words, in order to have a well-described system, number of the utilized plane waves must be clear. Truncating the number of plane waves is the cutoff energy. In this regard, equation (20) is the truncated plane wave:

$$\phi_k(r) = \sum_{G+k<G_{cut}} c_{k+G} \, exp[i(k+G)r] \quad (23)$$

The number of terms in this formula varies slightly depending on the value of k.

2.5.6 Pseudopotentials

Tightly bound core electrons in atoms oscillate on short length scales in real space due to the large potential running in this area. Therefore, the number of the plane waves needed for the calculations increases leading to time consuming calculations, which is problematic in DFT calculations. However, from a physical standpoint, core electrons are not very significant in determining chemical bonding and other physical features of materials and these characteristics are rather controlled by the less closely bonded valence electrons.

It was obvious from the beginning of the development of plane-wave methods that calculations approximating the characteristics of core electrons in such a way that fewer plane waves are required, to be significantly beneficial. One of the most important approaches in this regard is to use pseudopotentials which was introduced in 1934[72]. Pseudopotentials, in theory, substitute the electron density of a specific group of core electrons with a smoothed density designed to match many crucial physical and mathematical characteristics of the genuine ion core. Then, the electron characteristics in computations are fixed in an approximate method called the frozen core approximation. Computations that do not contain the frozen core approximation are called all-electron calculations. In other words, the pseudopotential is an effective potential designed to replace the atomic all-electron potential (full potential) in such a way that core states are eliminated, and the valence electrons are characterized by pseudowavefunctions with much fewer nodes.

Figure 2.2 illustrates the comparisons between the genuine wavefunction with pseudowavefunction.

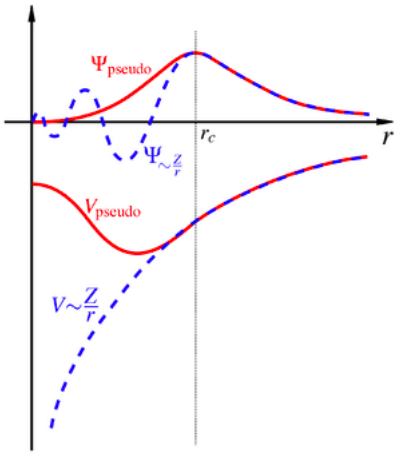

Figure 2.2 Nucleus Coulomb potential wavefunction (dashed blue line) and pseudopotential wavefunction (solid red line) comparison. Above a particular cutoff radius r_c, the genuine wavefunction and pseudowavefunctions and potentials coincide. (Source: https://en.wikipedia.org/wiki/Pseudopotential)

There are two different types of pseudopotentials. High-cutoff-energy required pseudopotentials are referred to as "hard," whereas low-cutoff-energy required pseudopotentials are referred to as "soft." Most pseudopotentials are defined using Vanderbilt's approach which are known as ultrasoft pseudopotentials (USPPs). They are called pseudopotentials because of the fact that they need far lower cutoff energies than competing methods do. One downside of employing USPPs is that constructing the pseudopotential for each atom necessitates the specification of a number of empirical factors. The projector augmented-wave (PAW) technique, first described by Blöchl and later extended for plane-wave computations by Kresse and Joubert[73], is another frozen core approach that overcomes some of the problems of USPPs. For tiny molecules and extended solids, Kresse and Joubert compared USPP, PAW, and all-electron computations extensively. Their findings reveal that properly constructed USPPs and the PAW technique provide nearly similar results in many circumstances, and that these results accord well with all-electron computations. The PAW method is more reliable than USPPs in materials with significant magnetic moments or atoms with big variations in electronegativity.

2.6 Importance of surfaces

Catalysis, interfaces, membranes for gas separations, and semiconductor manufacture all rely on surfaces for their functionality. There has been research showing a link between a surface's structure and its catalytic activity, highlighting the importance of understanding surface geometry and electronic structure. DFT has played a significant role in the development of three-way catalysts that decrease CO, NO_x, and SO_x emissions from automobiles, among other applications. Using DFT approaches, researchers have discovered the processes of catalytic reactions on metals, MOF zeolites, and oxides, which has led to advancements in the design of catalytic converters that increase their efficiency and cut their costs. DFT and surface science investigations have frequently worked together to provide effective results. Scanning tunneling microscopy (STM), temperature-programmed

desorption, X-ray diffraction, and X-ray photoelectron spectroscopy have all been used in conjunction with DFT to study the surface structure of metals, metal oxides, nanoparticles, carbides, and sulfides. Different atomic and molecular species' binding to surfaces, as well as surface properties, have been studied using DFT in conjunction with a wide range of experimental approaches. Several processes rely on the absence of oxygen atoms on the surface, and DFT simulations have shown that this is the case as well as explained the underlying physics.

Material that is infinite in two dimensions but finite along its surface normal is the optimal paradigm for studying a surface. In order to do this, periodic boundary conditions in two dimensions, but not in the third, may appear appropriate. This is best demonstrated in Figure 2.3 where the supercell only contains atoms that extend about one-fifth of the supercell's vertical length. The atoms in the supercell's bottom half occupy the whole area in x and y dimensions, but there is still vacant space above the atoms in the supercell's upper half. This model is known as the slab model because, when the supercell is replicated in all three dimensions, it forms a sequence of solid material slabs separated by empty areas. The void between periodic pictures of the slab along the z-axis is known as the vacuum space. Vacuum spacing must be sufficient to ensure that the electron density of the material drops off to zero in a vacuum such that one slab has little or no impact on the other.

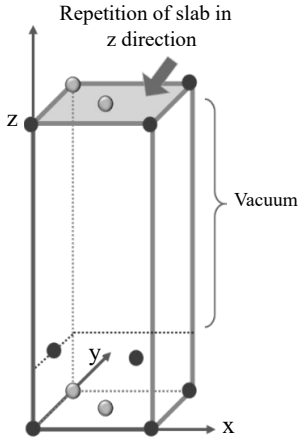

Figure 2.3 Supercell that, when utilized with periodic boundary conditions in all three directions, defines a material with a solid surface.

2.6.1 Choosing k points for surface calculations

Earlier, we addressed selecting k points for Brillouin zone integration. The Monkhorst–Pack technique for selecting k points may be utilised when selecting k points for slab and bulk computations, with many of the same issues applying. It is helpful to analyse the reciprocal lattice vectors corresponding to the supercell specified above in order to gain some idea regarding this task. Our supercell has one "short" dimension in reciprocal space because it has one "long" dimension in actual space meaning that for reciprocal integrals in the one direction, we may not require as many points to approximate them as we would need in the other two directions. The presence of a vacuum area in the long dimension of the supercell presents another valuable insight for k point selection. The electron density drops to zero at a short distance from the slab's edge if the vacuum zone is large enough. This indicates that utilising just one k point in the one direction, precise results are feasible.

3 Electrochemistry and concepts in catalysis

For the most part, the work given in this thesis focuses on the surface of an electrochemical environment at potentials close to zero, which is the reversible potential of the CH_3OH, $HCOOH/CO_2$ pair. Open systems such as surfaces in this environment are capable of exchanging neutral molecules, ions, and electrons with the environment. Further complicating factors include the presence of an electrolyte at the surface, which might alter the adsorbate structures produced there. To understand how oxide surfaces vary from metallic catalysts in terms of CO_2 reduction processes, we need to understand the atomistic mechanisms. To do so, the selectivity and activity of the surfaces are required to be explored. In this chapter, the concepts that are needed to drive selectivity and activity of the surfaces are discussed. Oxide surface binding energy characteristics have also been determined as a reference for optimal activity and selectivity for CO_2RR. In addition, scaling relations are used to construct activity volcanoes for CO_2RR on oxide surfaces.

3.1 Adsorption and reaction free energies

Reaction and adsorption energies can be estimated by calculating the difference in energy between a reference and a final state. In order to determine the adsorption of a species (A) on a surface, three calculations are necessary: one with species already adsorbed (A*), one with the surface alone (*), and one with the surface in the gas phase ($A_{(g)}$). The computed adsorption energy may be stated as follows, as a result:

$$\Delta G_A = G_{A*} - G_* - G_{A_{(g)}} \quad (1)$$

It is feasible to calculate the binding free energy of intermediates on a catalyst surface by making use of the free energy estimations of the surface both with and without the protonated adsorbate, in addition to the free energy of reference molecules. When there is no applied potential U, for instance, the binding free energy of AH* for the reaction $A^*+(H^++e^-) \rightarrow AH^*$ will be as equation (2),

$$\Delta G_{AH*}(U=0) = G_{AH*} - G_{A*} - \frac{1}{2}G_{H_2} \quad (2)$$

where, the protonated adsorbate's free energy is denoted by $G_{AH*}$and the free energy of H_2 molecules and A*, are denoted by G_{A*}, and G_{H_2}, respectively.

3.2 Statistical mechanics

Theoretically, DFT computations are carried out at absolute zero degrees Kelvin temperature (0K), although the pressure remains relatively undetermined. Thermodynamics and statistical mechanics are utilized in order to make the connection between the acquired energy and what may be observed in real-world scenarios. Our surface reactions are assumed to occur at ambient condition i.e., at temperature equal to 293 K and pressure equal to 1 atm. This indicates that we are in the isothermic-isobaric ensemble, in which Gibbs free energy should be minimized. This is provided by

$$G = U_{int} + PV - TS \quad (3)$$

where U_{int}, P, V, T, and S denote internal energy, pressure, volume, temperature, and entropy of the system, respectively. When calculating Gibbs free energy for adsorbates, we ignore the extremely minor changes in volume and use the Helmholtz free energy (H) illustrated as follows.

$$H = U_{int} - TS \quad (4)$$

As a result, we will be using Gibbs free energy rather than Helmholtz free energy for the entirety of the thesis.

3.3 Vibrational analysis

The molecules and adsorbates of interest tend to fluctuate in the region close to the energy minimum that is found while the system is relaxing. One way to look at this is to imagine bonds as being similar to springs that compensate for deviations from equilibrium. Calculations of vibrational frequencies enable the calculation of thermodynamic properties. Analyses of vibrational frequencies are based on the notion of small oscillations[74]. This relies on the assumption that the energy landscape is locally harmonic near equilibrium, which means that the vibration modes can be obtained by diagonalizing the mass-weighted Hessian matrix.

For the purpose of determining an adsorbate configuration's free energy, this thesis makes use of the relation that is presented below,

$$G(U = 0) = E_{DFT}(T = 0) + E_{ZPE} + \int_0^T C_p(T')dT' - T\mathrm{S} \quad (5)$$

where E_{DFT} is the energy obtained from DFT calculations, E_{ZPE} is the zero-point energy and C_p is the constant pressure specific heat. To compute the Gibbs binding free energy of an adsorbed intermediate from equation (5), we use the normal modes of vibration for several intermediates to determine zero-point energy, entropy, and the integral term[75]. As a result, the relations equation (6) and equation (7) have been employed.

$$E_{ZPE} = \frac{1}{2}\sum_i h\nu_i \quad (6)$$

$$-TS_{vib} + \int_0^T C_p(T')dT' = \sum_i \left(k_B T ln\left(1 - e^{-h\nu_i/k_B T}\right)\right) \quad (7)$$

Where h is the Plank constant, and k_B and ν_i are the Boltzmann constant and vibrational frequencies, respectively. The thermodynamic tables have been used to obtain zero-point energy, TS_{vib} and C_p for molecules.

3.4 Reference electrodes

Utilizing an equilibrium reaction that is already known allows for the construction of a reference electrode. When the reference has been established, the subsequent reactions can relate to this. The normal hydrogen electrode, also known as the NHE, has traditionally been used as a reference potential. This electrode is defined as the equilibrium for hydrogen gas

as well as free protons and electrons when it is placed in a 1N acid solution on platinum at a temperature of 298K and a pressure of 1 atm[76].

It has recently come to light that the thermodynamic activity of hydrogen ions is a more suitable reference, and the electrode that measures this activity is known as the standard hydrogen electrode (SHE). Although it is impossible to construct such an electrode, the material might serve as the foundation for electrode tables. When the reaction contains hydrogen evolution or oxidation half reactions, the electrode potential is pH-dependent because the Nernst equation takes into consideration the concentration of hydrogen. As a result, the reversible hydrogen electrode, also known as the RHE, is defined as the potential shift that is incorporated in the potential itself[77].

$$U_{RHE} = U_{SHE} + \frac{k_B T}{eln10} pH \quad (8)$$

3.5 Computational hydrogen electrode model

Doing a calculation to determine the free energy of adsorption for electrochemical reaction intermediates in a real electrochemical system can be an extremely difficult task, due to the presence of electrolyte molecules and an electric field. It is exceedingly computationally costly to simulate such a large number of adsorbate/catalyst surface variants with all of the electrolyte-catalyst interface properties. The computational hydrogen electrode (CHE)[31] model is a method that may be utilized to approximate the free energy of an electrochemical reaction when the reaction is carried out at a specific voltage. The reaction free energy of the electrochemical system is estimated at a certain potential U by subtracting the reaction free energy calculated without explicitly addressing potential or electrolyte. The model shows a clear linear relationship between the reaction free energy of each step involving a coupled electron-proton transfer and the applied potential U,

$$\Delta G_{AH}(U) = \Delta G_{AH}(U = 0) + eU \quad (9)$$

where e is the elementary charge.

3.6 Scaling relation

In a broader sense, it has been established that the binding energies of many intermediates that interact with the surface via the same atom or atoms scale with one another. These intermediates are responsible for the surface interactions. To put it another way, simulations conducted with density functional theory have shown that the binding energy of any particular adsorbate scales approximately with the binding energy of the core atom[78]. This event arises as a result of the core atom's primary interaction, which is a direct chemical bonding with the surface of the catalyst. Within the realm of theoretical catalysis, these reported linear relationships between the energy of adsorbates and the binding energy of the central atom are referred to as scaling relations. Scaling relations are linear relationships that relate the energy of adsorbates to the binding energy of the central atom[78–80]. For instance, Figure 3.1 a and b illustrate the scaling relationship between the OH* and CH_3O* and H_2COOH* vs OH* intermediates that interact with the surface via oxygen atoms, respectively.

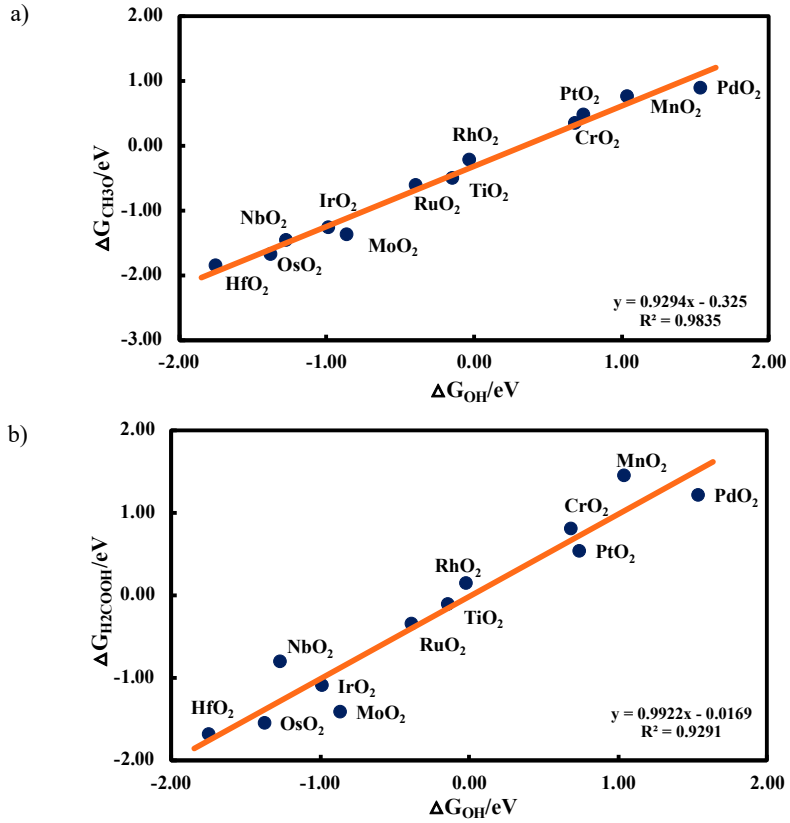

Figure 3.1 Scaling relation for a) CH_3O vs OH and b) H_2COOH vs OH[81]

3.7 Theoretical volcano concept

The empirical law of Sabatier claims that given a process, there is an ideal binding energy for an intermediate, where stronger and weaker binding leads to a lower level of activity for the reaction. For a simple reaction like HER, the volcano-shaped correlation between activity and binding energy is self-evident[82]. If the hydrogen atom is too loosely bound to the surface, it is inefficient to produce H*; if it is too tightly bound, removing H* to synthesis hydrogen gas requires an excessive amount of energy. However, due to the huge number of adsorbates and potential paths, the connection between adsorbate binding energies and total activity is counterintuitive for a complicated reaction like CO_2RR. Simple linear relations based on scaling rules contribute to the decomposition of this complexity. By exploiting the connection between the binding energies of various adsorbates, the activity may be represented as a function of just one or two binding energy parameters. Finally, such a simplification results in a binding energy–activity connection like that of a volcano, comparable to Sabatier's idea of a volcano. The binding energy, to which all other binding energy characteristics and activity may be correlated, is frequently referred to as the descriptor for the catalytic process.

3.7.1 How to construct a theoretical volcano

Numerous single electron-proton transfer steps make up the reaction process. The inherent binding free energies of the intermediates before and after protonation determine the free energy change for such steps. Additionally, the applied electrochemical potential, which is

modeled using the computational hydrogen electrode model in here, modifies the free energy change. Calculating binding energy offers the free energy required to progress an elementary reaction step and estimates the potential at which the reaction step can occur. Then, the binding free energy of adsorbates can be specified as a function of OH* binding energy, using linear scaling relations, which enables expressing the thermodynamically limiting potential as a linear function of OH* binding energy for every single electrochemical step. Considering the two main CO_2RR products i.e., formic acid and methanol, investigated throughout this thesis, theoretical volcanos can be constructed as follows.

3.7.1.1 Formic acid formation volcano

The first two electron-proton transfer steps in CO_2RR may lead to formic acid formation that involves OHCO* as the only surface bound intermediate.

$$CO_2(g) + * + (H^+ + e^-) \rightarrow OCHO* \quad (10)$$

$$OCHO* + (H^+ + e^-) \rightarrow HCOOH(aq) \quad (11)$$

The onset potential of these two fundamental steps is parametrized using its linear scaling relation with OH* binding and as a result, formic acid volcano is constructed consisting of only two lines/legs (CO_2 → OCHO*: right leg of volcano and OCHO* → HCOOH(aq): left leg of volcano) shown in figure 3.2 a. The slope of the OH*-OCHO* functional relationship is nearly one, which means that catalysts with weaker OH* adsorption have easier OCHO* protonation than formic acid evolution and therefore the right leg of the volcano becomes their potential determining step. However, strong bonding of OH* on catalysts surfaces results in easier release of formic acid over OCHO* protonation and hence, the left leg of the volcano becomes their potential determining step. The volcano's summit almost meets the equilibrium potential line indicating a catalyst surface with ~0 eV binding free energy at 0 V_{RHE} for OH* and OCHO* being an ideal candidate to evolve formic acid with almost no required overpotential.

3.7.1.2 Methanol formation volcano

In CO_2RR, methanol formation is a six-step proton-electron transfer process as the mechanism follows.

$$OCHO* + (H^+ + e^-) \rightarrow HCOOH* \quad (12a)$$

or

$$OCHO* + (H^+ + e^-) \rightarrow HCOOH(aq) + * \quad (12b)$$

$$HCOOH* + (H^+ + e^-) \rightarrow H_2COOH* \quad (13a)$$

or

$$HCOOH(aq) + (H^+ + e^-) \rightarrow H_2COOH* \quad (13b)$$

$$H_2COOH* + (H^+ + e^-) \rightarrow H_3CO* + OH* \quad (14a)$$

or

$$H_2COOH* + (H^+ + e^-) \rightarrow H_2CO* + H_2O(l) \quad (14b)$$

$$H_3CO* + OH* + (H^+ + e^-) \rightarrow H_3CO* + H_2O(l) \quad (15a)$$

or

$$H_2CO^* + (H^+ + e^-) \rightarrow H_3CO^* \quad (15b)$$

$$H_3CO^* + (H^+ + e^-) \rightarrow H_3COH(aq) + * \quad (16)$$

As discussed before, each reaction step corresponds to a line/leg in the volcano plot. Methanol formation volcano in this regard was initially made up of six limiting potentials, each representing a particular reaction step in the overall process. For simplicity all the reaction steps have been removed except for the elementary steps that are potential determining steps for methanol formation and the resulting volcano is shown in Figure 3.2 b. The potential determining steps in this volcano are OH* removal (OH* → $H_2O(l)$), OCHO* removal (OCHO* → HCOOH*) and HCOOH(aq) activation (HCOOH(aq) → H_2COOH^*) as they are the steps requiring the least reducing potential.

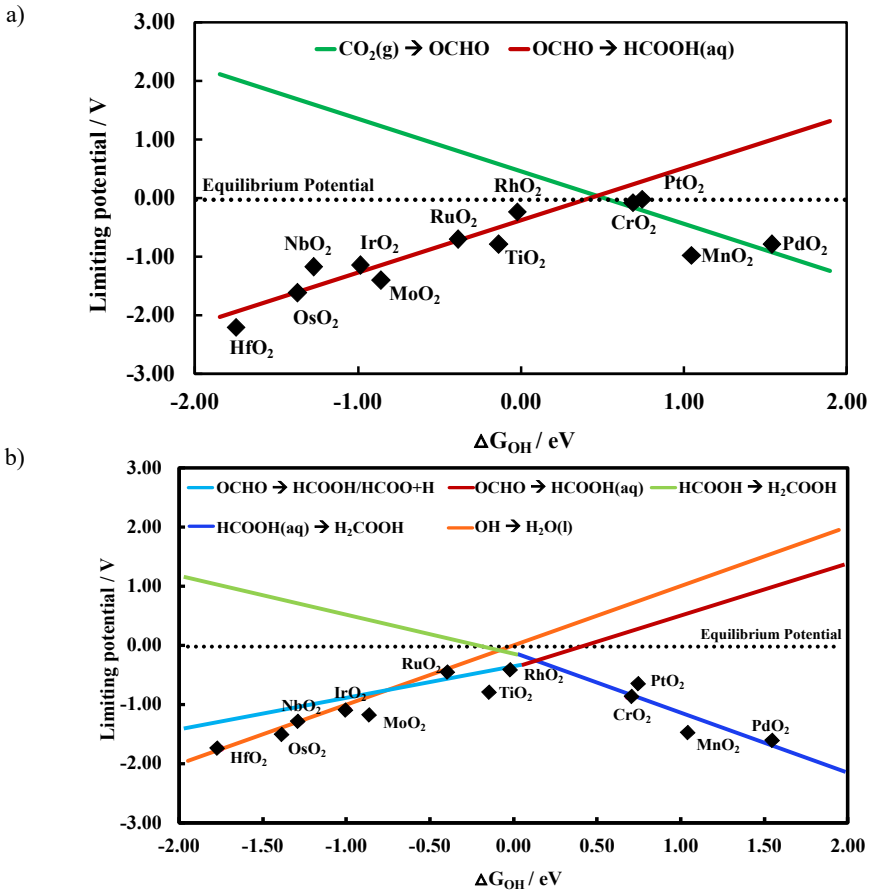

Figure 3.2 Theoretical volcano for formation of a) formic acid and b) methanol from scaling relations[81].

3.8 Stability of the TMOs under CO_2RR condition

The electrochemical reduction of CO_2 holds promise as a means of converting CO_2 into valuable chemicals and fuels using renewable energy sources. However, the process is complex and requires electrocatalysts that are both efficient and stable. Marcel Pourbaix has developed a unique and concise method of summarizing the corrosion thermodynamic information and the stability of different forms of different metals in contact with water as a

function of applied electric potential and pH of the solution[83]. These Pourbaix diagrams indicate particular potential and pH regions, where the metal undergoes phase transformation and other potential and pH windows, where the metal is retained intact. According to Pourbaix diagrams taken form Factsage TM (https://www.factsage.com/), ruthenium maintains its stability as RuO_2 under potentials ranging from 0.6 to 1.4 V at pH=0 and -0.3 to 0.6 V at pH=14 (see Table 3.1), but undergoes transformation into Ru under more negative potentials across all pH ranges. HfO_2 exhibits stability at negative potentials until -1.5 V at pH = 0 and until -2.4 V at pH = 14. MoO_2 remains stable under potentials of -0.1 to 0.6 V at pH=0 and at around -1.0 V at pH=14. RhO_2 shows stability under potentials greater than 0.8 V at pH=0 and greater than 0.0 V at pH=14. OsO_2 retains stability under potentials of 0.6 to 1.0 V at pH=0 and -0.2 to 0.2 V at pH=14. IrO_2 stays stable under potentials greater than 0.7 V at pH=0 and in the potential range of -0.1 to 1.5 V at pH=14. However, MoO_2, RhO_2, OsO_2, and IrO_2 transform to metallic form across all pH ranges as the potential shifts towards more negative values than indicated in Table 3.1. NbO_2 retains its stability under negative potentials of -0.6 to -0.3 V at pH=0 and -1.4 to -1.0 V at pH=14 but it undergoes transformations to NbO and Nb under other pH values and potentials. Titanium is solely stable as TiO_2 at potentials greater than -0.5 V and -1.4 V at pH=0 and 14, respectively, while under all pH values below this threshold, it transforms into TiH_2. Similarly, Zirconium is stable as ZrO_2 at negative potentials and pH above ~8 but it transforms to ZrH_2 for pH below 8. CrO_2 and PtO_2 exhibit no stability under any potential or pH values. MnO_2 is stable only within a narrow window of positive potentials of 1.4 to 1.6 V at pH=0 and 0.1 to 0.5 V at pH=14 and undergoes transformation into different forms depending on the pH and under negative potentials. PdO_2 remains stable under positive potentials regardless of the pH; however, under potentials ranging from 0 to -1.5 V, it transforms into PdO, while at more negative potentials, it transforms into metallic Pd. SnO_2 exhibits stability at potentials above 0 V under all pH ranges except at pH=~14, but it undergoes transformations into different forms under potentials below 0 V based on the pH conditions. Table 3.1 summarizes metal oxide stability at particular potentials at pH = 0 and 14.

Table 3.1 Potential range where the metal dioxide in rutile structure is predicted to be stable according to Pourbaix diagram analysis, shown at pH= 0 and 14.

Metal oxide	Potential (V) at pH=0	Potential (V) at pH=14
HfO_2	≥ -1.5	≥ -2.4
MoO_2	-0.1 to 0.6	-1.0
RuO_2	0.6 to 1.4	-0.3 to 0.6
RhO_2	≥ 0.8	≥ 0.0
OsO_2	0.6 to 1.0	-0.2 to 0.2
IrO_2	≥ 0.7	-0.1 to 1.5
NbO_2	-0.6 to -0.3	-1.4 to -1.0
TiO_2	≥ -0.5	≥ -1.4
ZrO_2	----	≥ -1.6
CrO_2	----	----
PtO_2	----	----
PdO_2	≥ 1.1	≥ 0.2
SnO_2	≥ 0.0	----
MnO_2	1.4 to 1.6	0.1 to 0.5

Although it may seem that most of the metal oxides studied in the current work are not stable in negative potentials, most of them are reported to be stable in an electrochemical cell under reducing conditions according to carried out studies. These observations could be due to the effect of adsorbates on the surface or the modifications to these metal oxides, such as using substrates or doping. Also, when the metal oxide surface has been created, it may be stable or metastable when used in electrochemical cell at reducing conditions, even at potential values more negative than the Pourbaix analysis predicts. Following studies have focused on investigating the stability of transition metal oxides under electrochemical reduction conditions.

Among the transition metal oxides, RuO_2 and IrO_2 have received considerable attention as electrocatalysts for CO_2 reduction due to their catalytic activity, stability, and low overpotential for converting CO_2 [22,23,84,85]. While other transition metal oxides considered in our studies have also shown promising catalytic activity for CO_2 reduction, their stability under CO_2 reduction conditions is less well studied. SnO_2 is reported to be a selective catalyst in CO_2RR, but its stability under CO_2RR conditions is not well understood. One study reported that SnO_2 undergoes self-reduction under reduction condition[87]. Li et al.[88], conducted a study on CuO–HfO_2 interface toward enhanced CO_2 electroreduction to C_2H_4. According to them, the selection of HfO_2 as the interface material is based on its advantageous attributes, including cost-effectiveness, superior thermal and chemical stability, robust mechanical properties, a high level of surface basicity, and remarkable ability to adsorb CO_2 and that HfO_2 plays a central role in stabilizing Cu^+. PdO_2 on the other hand, is reported to be unstable at cathodic potential range and decomposes to PdO. PdO is also unstable, leaving bare Pd sites available for the reaction[89]. Moreover, RhO_2 is also reported to be unstable, but it can be stabilized by compressive strain. The researchers accomplished this by creating a strawberry-like structure containing RhO_2 clusters embedded in the surface layer of Rh nanoparticles[90]. The incompatibility between the oxide cluster and the metal substrate induces intense compressive strain, which helps to maintain the stability of the RhO_2 clusters at a reduction potential. Additionally, the stability of TiO_2 [91] and MoO_2 [92,93] under reducing conditions and the stability of Pt/PtO_2 electrode for HER [94] has been confirmed. MnO_2 nanosheets supported on nickel foam (MnO_2−NS/NF) [95] are also reported to be stable under CO_2RR condition.

4 Summary of Papers

4.1 Paper I

In the first paper density functional theory-based simulations are used to investigate the influence of solvent on the stability of intermediates in the CO_2 reduction reaction (CO_2RR) toward methanol and formic acid production and the inevitable competing hydrogen evolution reaction (HER) on 12 different transition metal oxides (TMOs). TMOs considered in this work are RuO_2, IrO_2, TiO_2, NbO_2, MoO_2, OsO_2, ZrO_2, RhO_2, PtO_2, MnO_2 and PdO_2. When calculating the free energy of adsorbates, one monolayer of water is added to improve the model system and compared to the results when water is not present in the computations. Limiting potential volcano plots for products are derived using adsorbate scaling relations, with an emphasis on catalytic trends. According to our findings, in the improved model system, cooperatively adsorbing (co-adsorbing) water alters the overpotentials for the formation of formic acid and methanol, which range from 0.2 to 0.5 V, respectively. Furthermore, co-adsorbed water results in destabilization of HCOOH on TMOs, except for IrO_2 and ZrO_2, and thus when the model system is enhanced, the selectivity shifts more toward formic acid than methanol. Moreover, recent experimental observations show that the RuO_2 catalyst is selective for HER are validated by the results of this study. In addition, other TMOs, such as MoO_2, ZrO_2, and OsO_2, are anticipated to reduce CO_2 to CO on their surfaces, whereas NbO_2 is predicted to be selective for formic acid and methanol production.

4.2 Paper II

In the second paper, the effect of changing CO coverage on CO_2 reduction reaction (CO_2RR) selectivity and activity toward methanol and formic acid production on 12 distinct transition metal oxide (TMO) surfaces is studied using density functional theory. The considered TMOs in this study are RuO_2, IrO_2, TiO_2, NbO_2, MoO_2, OsO_2, HfO_2, RhO_2, PtO_2, MnO_2 and PdO_2. Using scaling relation of adsorbed intermediates activity and selectivity volcanos for various products are constructed as CO coverage varies. We discovered that CO_2RR selectivity towards methanol, formic acid, and H_2 may be modified by altering the CO coverage on TMO surfaces. Accordingly, formic acid and methanol production overpotentials are reduced to an ideal level for all TMOs in this investigation when CO coverage is 50%. Overpotentials for converting CO_2 to methanol using MoO_2 and HfO_2 are predicted to be lower than those with 25% CO coverage. Moreover, our findings show that increased CO coverage on TMOs can slightly decrease the hydrogen evolution reaction (HER). The work shows that a moderate quantity of CO coverage on TMO surfaces is required to reduce methanol formation overpotentials. Since CO repulsion interactions alter adsorbate binding free energy, increased CO coverage on most TMOs leads in reduced overpotentials for formic acid production. Lastly, the current study reveals the relevance of the reaction conditions for the electrocatalytic conversion of CO_2 to liquid fuels utilizing TMO-based electrocatalytic systems.

4.3 Paper III

In this study, utilizing Density Functional Theory (DFT) calculations, we analyze and identify the active sites responsible for CO_2 reduction reaction (CO_2RR) towards CO and formic acid on TiO_2/RuO_2 and SnO_2/RuO_2 alloys with a rutile structure and (110) facet. To gain insight into catalytic active sites, Ti and Sn atoms in TiO_2 and SnO_2 catalysts are substituted with Ru atoms of varying ratios and compositions, in line with recent experimental trends. We construct volcano plots to predict the overpotential required for CO_2RR on all model systems. Our analysis indicates that catalyst compositions featuring alternating Ru-Ti binding sites for key intermediates of COOH or OCHO lead to higher overpotentials than the reference RuO_2 surface, which only produces H_2 experimentally. Conversely, if the binding sites are Ru-Ru or Ti-Ti, the overpotentials for CO formation are significantly reduced, indicating that these are the active sites of TiO_2/RuO_2 alloys. Regarding formic acid formation, the Ru-Ru sites result in the lowest overpotentials, while the Ti-Ti binding sites bind the OCHO intermediate too strongly, resulting in large overpotentials. Our calculations clearly indicate that replacing one Ru atom in a RuO_2 overlayer on TiO_2 with Cu significantly reduces the overpotential towards formic acid and CO formation, consistent with experimental observations. Additionally, in SnO_2/RuO_2 alloys, replacing Sn with Ru in the coordinatively unsaturated sites leads to a decreased overpotential compared to other model systems. This is likely due to electronic effects as key intermediates are catalyzed on neighboring bridge sites. In summary, our findings suggest that the knowledge gained from these synergistic effects can be used to engineer the active sites of these alloys to improve selectivity and reduce the required overpotential for CO_2RR.

5 Conclusion and outlook

5.1 Conclusion

This thesis investigates electrochemical CO_2 reduction reactions on transition metal oxides in detail in order to gain a deeper understanding of reaction mechanisms as well as to identify promising oxide electrocatalysts and approaches to engineer them. To calculate the free energy of adsorbed intermediates in CO_2RR toward formic acid and methanol formation and estimate the effect of solvent, we employed a simplified interface model with a single water layer. The co-adsorbed water has an effect on the interaction between each CO_2RR intermediate and the TMO surfaces, altering the overpotentials while leaving the potential-determining steps unchanged. In all cases, the presence of water molecules increases the overpotentials of products ranging from 0.2 V to 0.5 V, with the exception of MoO_2, for which the overpotential decreases by 0.2 V. Additionally, the presence of co-adsorbed water destabilizes HCOOH on surfaces. Moreover, the presence of HCOOH on the surface is essential for CO_2RR to proceed toward methanol formation; thus, its destabilization shifts the selectivity of methanol formation from a region near the top of the volcano to a less active region close to RuO_2 and IrO_2 compared to when co-adsorbed water is not included. In addition to the effect of solvent, we also investigate the effect of CO coverage. Therein, the effect of varying CO coverage on CO_2RR selectivity and activity volcanoes for formic acid and methanol formation on 12 transition metal oxide catalysts was studied. Comparing CO coverages show that 25% and 50% are good for methanol formation and 50% CO is more efficient for methanol formation with lower overpotentials. If CO coverage reaches 75%, formic acid is more selective. Comparing 25% CO coverage to 50% and 75% CO coverage, smaller repulsion exists between CO adsorbate and intermediates adsorbed on TMO surfaces, leading to higher methanol formation overpotentials in CO_2RR. For 75% CO coverage, the repulsion between CO adsorbates increases, weakening the binding free energy of intermediates adsorbed on the surface and forcing OCHO, which binds bidentate, to bind monodentate through one oxygen atom on the surface. Thus, formic acid forms, preventing methanol formation. It has been found that HfO_2, NbO_2, OsO_2, MoO_2 and IrO_2 can proceed to methanol formation due to a high OCHO and HCOOH binding free energy while NbO_2, OsO_2, and IrO_2 have a close OCHO binding free energy to that of H, which suppresses methanol production. Finally, all previous research suggests that transition metal alloys should be considered as potential CO_2RR catalysts. We discovered that the doped atoms in the surface layer of TMO alloy catalysts play a crucial role as active sites and determine the intermediate's binding free energies. Additionally, our results are consistent with studies that have reported the onset potentials and selectivity of CO(g), formate, and hydrogen on SnO_2 and RuO_2 electrodes.

In summary, our results predict new catalysts and conditions that benefit both theoreticians and experimentalists. The experiments will benefit from the screening results of several transition metal oxides in our studies to narrow down their span of focus to the introduced promising candidates of our findings for further investigations. This matter will immensely diminish the financial burden on these experiments and save the allocated hours on designing and testing of different catalysts. Our findings seek to reignite theoretical research efforts in the domain of oxide CO_2RR electrocatalysts by presenting a mechanistic knowledge of reaction mechanism, thermodynamic limitations, descriptors, and chemical variables

determining activity. Further, these findings contribute to the rational design of catalysts with higher efficiencies and lower required overpotentials toward the desired materials. Throughout the studies carried out in our last work, we have obtained a great insight and understanding of a recent experiment on RuO_2-based alloys. We have also been able to reproduce the results from this experiment which confirms the reliability of our findings to be used as a benchmark for further research and analysis. Lastly, the theoretical work presented in this thesis will serve as a guideline for the search of metal oxide-based alloys as catalysts for energy and sustainability. While the results of this thesis allow the rational design of a promising catalyst that permits employing CO_2 as a reactant to produce hydrocarbon-based products, this is one step forward in reducing the hazardous CO_2 emissions and ultimately tackling the biggest concern of humanity, global warming.

5.2 Outlook

The need for materials with better properties, lower costs, and less environmental impact has become a significant factor in the evolution of products and technologies[96]. In this direction, ceramic materials are crucial for a variety of applications, including sensors[97,98] radiation detectors[99], and catalysts[100,101]. High Entropy Oxides (HEO), or more specifically Entropy Stabilized Oxides (ESO), are unexplored ceramics with intriguing properties. Five or more elemental components may be arbitrarily arranged in a single lattice, and it has been suggested that the entropic influence on the free energy, and not the cohesive energy, is what determines thermodynamic stability[102]. Along with the development of high-entropy oxides, there was an increase in the number of studies conducted on various types of ceramics[103,104]. Rost et al.[102] investigated Entropy Stabilized Oxides (ESO), a new class of thermodynamically similar materials to High Entropy Alloys (HEA)[105,106]. This was a significant advancement in materials science. Because of how well they crystallized, how flexible they were, and how well they resisted corrosion and wear, HEAs received considerable attention[107–109]. Due to the study of HEAs, it became possible to examine the central regions of phase diagrams[110].

From a catalytic standpoint, the field of designing oxide-based materials with high entropy is not yet fully developed. To expand the HEO engineering field, a strategic plan that takes into account the following factors is required: a) During the formation of HEO, the enthalpy of mixing and configurational entropy assess the probability of a real HEO formation. A high enthalpy indicates that the structures could separate or cluster, whereas an increase in the number of cations increases their entropy stabilization. The entropy stabilization process can be examined by subjecting the material to a calcination treatment at both low and high temperatures and observing if a single phase is produced[111]. For this type of experiment, both rock-salt structures (R-HEO) and fluorite structures (F-HEO) have been proposed. b) When selecting the elements that will comprise the compound, the valence of the cations and their compatibility with the other elements are two crucial considerations. By coordination environment compatibility, we imply that the size of the cations must be suitable for the oxygen sub-lattice and that the structural tolerance factor must also be satisfied[102,112]. Likewise, the valence of the cations should be set so as to maintain charge equilibrium. Even though HEO is a new family of materials, a substantial amount of research is conducted on combining cations with the same valence. By moving in the direction of combining cations with different valences, it may be possible to create new materials with unprecedented properties and catalytic performance. The term for this is "charge distortion."

This is because different valence metals and oxygen do not share their electron clouds in the same way. Various catalytic reactions, such as the reduction of CO_2 to various hydrocarbons[113,114], and the reforming of hydrocarbons, are likely to be impacted differently by this type of electron cloud distortion. As a result of their naturally distorted lattices, HEO can be used as catalysts or as catalyst supports (decorated with active metal).

The work presented in this thesis shows that the classification of CO_2RR products based on a catalyst's O, C and, H affinities leads to the notion that by alloying with specific O-binding, C-binding or H-binding sites, metal oxide-based alloys can be designed to have one or two active sites with tuned binding energies for key reaction intermediates. This is the subject of our group's current research. Currently, we are employing high-throughput screening techniques for multi-principal component-based alloy catalysts to identify those catalysts selective for methanol production from CO_2.

References

1 J. Houghton, *Reports Prog. Phys.*, 2005, **68**, 1343.

2 D. Archer, *J. Geophys. Res. Ocean.*, 2005, **110**, 1.

3 A. Montenegro, V. Brovkin, M. Eby, D. Archer and A. J. Weaver, *Geophys. Res. Lett.*, 2007, **34**, 1.

4 P. Friedlingstein and S. Solomon, *Proc. Natl. Acad. Sci. U. S. A.*, 2005, **102**, 10832.

5 G. A. Olah, *Angew. Chemie Int. Ed.*, 2005, **44**, 2636.

6 G. A. Olah and G. K. S. Prakash, US patent 5928806, 1999.

7 George A. Olah, *Chem. Eng. News*, 2003, **81**, 5.

8 G. A. Olah, *Chem. Eng. News*, 2003, **81**, 42.

9 G. A. Olah, *Catal. Lett. 2004 931*, 2004, **93**, 1.

10 X. Lim, *Nature*, 2015, **526**, 628.

11 Y. Y. Birdja, E. Pérez-Gallent, M. C. Figueiredo, A. J. Göttle, F. Calle-Vallejo and M. T. M. Koper, *Nat. Energy*, 2019, **4**, 732.

12 J. F. Hull, Y. Himeda, W. H. Wang, B. Hashiguchi, R. Periana, D. J. Szalda, J. T. Muckerman and E. Fujita, *Nat. Chem.*, 2012, **4**, 383.

13 C. Costentin, S. Drouet, M. Robert and J. M. Savéant, *Science*, 2012, **338**, 90.

14 M. D. Sampson, A. D. Nguyen, K. A. Grice, C. E. Moore, A. L. Rheingold and C. P. Kubiak, *J. Am. Chem. Soc.*, 2014, **136**, 5460.

15 Y. Hori, K. Kikuchi and S. Suzuki, 2006, **14**, 1695.

16 Y. Hori, A. Murata and R. Takahashi, *J. Chem. Soc. Faraday Trans. 1*, 1989, **85**, 2309.

17 Y. Hori, *Mod. Asp. Electrochem.*, 2008, **42**, 89.

18 K. P. Kuhl, T. Hatsukade, E. R. Cave, D. N. Abram, J. Kibsgaard and T. F. Jaramillo, *J. Am. Chem. Soc.*, 2014, **136**, 14107.

19 A. Bandi, *J. Electrochem. Soc.*, 1990, **137**, 2157.

20 A. Bandi and H. -M. Kühne, *J. Electrochem. Soc.*, 1992, **139**, 1605.

21 N. Spataru, K. Tokuhiro, C. Terashima, T. N. Rao and A. Fujishima, *J. Appl. Electrochem.*, 2003, **33**, 1205.

22 J. Qu, X. Zhang, Y. Wang and C. Xie, *Electrochim. Acta*, 2005, **50**, 3576.

23 J. P. Popić, M. L. Avramov-Ivić and N. B. Vuković, *J. Electroanal. Chem.*, 1997, **421**, 105.

24 J. Hussain, H. Jónsson and E. Skúlason, *ACS Catal.*, 2018, **8**, 5240.

25 S. Mezzavilla, Y. Katayama, R. Rao, J. Hwang, A. Regoutz, Y. Shao-Horn, I. Chorkendorff and I. E. L. Stephens, *J. Phys. Chem. C*, 2019, **123**, 17765.

26 I. M. Kodintsev and S. Trasatti, *Electrochim. Acta*, 1994, **39**, 1803.

27 T. Reier, H. N. Nong, D. Teschner, R. Schlögl and P. Strasser, *Adv. Energy Mater.*, 2017, **7**, 1.

28 M. Karamad, H. A. Hansen, J. Rossmeisl and J. K. Nørskov, *ACS Catal.*, 2015, **5**, 4075.

29 A. Bhowmik, H. A. Hansen and T. Vegge, *ACS Catal.*, 2017, **7**, 8502.

30 E. Tayyebi, J. Hussain, Y. Abghoui and E. Skúlason, *J. Phys. Chem. C*, 2018, **122**, 10078.

31 J. K. Nørskov, J. Rossmeisl, A. Logadottir, L. Lindqvist, J. R. Kitchin, T. Bligaard and H. Jónsson, *J. Phys. Chem. B*, 2004, **108**, 17886.

32 M. A. Henderson, *Surf. Sci. Rep.*, 2002, **46**, 1.

33 A. Lobo and H. Conrad, *Surf. Sci.*, 2003, **523**, 279.

34 M. A. Henderson, *Surf. Sci.*, 1996, **355**, 151.

35 P. J. Feibelman, *Science*, 2002, **295**, 99.

36 H. Ogasawara, B. Brena, D. Nordlund, M. Nyberg, A. Pelmenschikov, L. G. M. Pettersson and A. Nilsson, *Phys. Rev. Lett.*, 2002, **89**, 276102.

37 S. Schnur and A. Groß, *New J. Phys.*, 2009, **11**, 125003.

38 X. Lin and A. Groß, *Surf. Sci.*, 2012, **606**, 886.

39 N. Atrak, E. Tayyebi and E. Skúlason, *Appl. Surf. Sci.*, 2021, **570**, 151031.

40 K. P. Kuhl, T. Hatsukade, E. R. Cave, D. N. Abram, J. Kibsgaard and T. F. Jaramillo, *J. Am. Chem. Soc.*, 2014, **136**, 14107.

41 A. A. Peterson, F. Abild-Pedersen, F. Studt, J. Rossmeisl and J. K. Nørskov, *Energy Environ. Sci.*, 2010, **3**, 1311.

42 A. A. Peterson and J. K. Nørskov, *J. Phys. Chem. Lett.*, 2012, **3**, 251.

43 J. Rossmeisl, Z. W. Qu, H. Zhu, G. J. Kroes and J. K. Nørskov, *J. Electroanal. Chem.*, 2007, **607**, 83.

44 S. Siahrostami and A. Vojvodic, *J. Phys. Chem. C*, 2015, **119**, 1032.

45 E. Skúlason, V. Tripkovic, M. E. Björketun, S. Gudmundsdóttir, G. Karlberg, J. Rossmeisl, T. Bligaard, H. Jónsson and J. K. Nørskov, *J. Phys. Chem. C*, 2010, **114**, 18182.

46 E. Tayyebi, Y. Abghoui and E. Skúlason, *ACS Catal.*, 2019, **9**, 11137.

47 R. Mu, Z. J. Zhao, Z. Dohnálek and J. Gong, *Chem. Soc. Rev.*, 2017, **46**, 1785.

48 J. Lee, D. C. Sorescu, X. Deng and K. D. Jordan, *J. Phys. Chem. Lett.*, 2013, **4**, 53.

49 X. Lin and A. Groß, *Surf. Sci.*, 2012, **606**, 886.

50 E. Schrödinger, *Phys. Rev.*, 1926, **28**, 1049.

51 D. C. Young, 2001, 381, ISBN: 978-0471333685.

52 K. I. Ramachandran, G. Deepa and K. Namboori, *Comput. Chem. Mol. Model. Princ. Appl.*, 2008, 1, ISBN: 978-3540773047.

53 M. Born and R. Oppenheimer, *Ann. Phys.*, 1927, **389**, 457.

54 W. Kohn and L. J. Sham, *Phys. Rev.*, 1965, **140**, A1133.

55 P. Hohenberg and W. Kohn, *Phys. Rev.*, 1964, **136**, B864.

56 W. J. Hehre, 2003, 1, ISBN: 978-1890661182.

57 P. W. Atkins and R. Friedman, 1997, 545, ISBN: 978-0199541423.

58 D. S. Sholl and J. A. Steckel, 2009, 1, ISBN: 978-0470373170.

59 D. M. Ceperley and B. J. Alder, *Phys. Rev. Lett.*, 1980, **45**, 566.

60 J. P. Perdew and W. Yue, *Phys. Rev. B. Condens. Matter*, 1986, **33**, 8800.

61 J. P. Perdew, J. A. Chevary, S. H. Vosko, K. A. Jackson, M. R. Pederson, D. J. Singh and C. Fiolhais, *Phys. Rev. B*, 1992, **46**, 6671.

62 J. P. Perdew, J. A. Chevary, S. H. Vosko, K. A. Jackson, M. R. Pederson, D. J. Singh and C. Fiolhais, *Phys. Rev. B*, 1993, **48**, 4978.

63 J. Wellendorff, K. T. Lundgaard, A. Møgelhøj, V. Petzold, D. D. Landis, J. K. Nørskov, T.

Bligaard and K. W. Jacobsen, *Phys. Rev. B - Condens. Matter Mater. Phys.*, 2012, **85**, 235149.

64 A. Sommerfeld and H. Bethe, 1933, 333, ISBN: 978-3642892608.

65 J. C. Slater, *Rev. Mod. Phys.*, 1934, **6**, 209.

66 P. Kratzer and J. Neugebauer, *Front. Chem.*, 2019, **7**, 106.

67 O. Jepson and O. K. Anderson, *Solid State Commun.*, 1971, **9**, 1763.

68 A. Baldereschi, *Phys. Rev. B*, 1973, **7**, 5212.

69 D. J. Chadi and M. L. Cohen, *Phys. Rev. B*, 1973, **8**, 5747.

70 S. L. Cunningham, *Phys. Rev. B*, 1974, **10**, 4988.

71 H. J. Monkhorst and J. D. Pack, *Phys. Rev. B*, 1976, **13**, 5188.

72 H. Hellmann, *J. Chem. Phys.*, 2004, **3**, 61.

73 G. Kresse and D. Joubert, *Phys. Rev. B*, 1999, **59**, 1758.

74 H. Goldstein, C. P. Poole and J. L. Safko, 2002, ISBN:978-0201657029.

75 D. A. McQuarrie, 1983, ISBN: 978-0935702132.

76 G. Inzelt, A. Lewenstam and F. Scholz, 2013, 1, ISBN: 978-3642361883.

77 Y. Cai and A. B. Anderson, *J. Phys. Chem. B*, 2004, **108**, 9829.

78 F. Abild-Pedersen, J. Greeley, F. Studt, J. Rossmeisl, T. R. Munter, P. G. Moses, E. Skúlason, T. Bligaard and J. K. Nørskov, *Phys. Rev. Lett.*, 2007, **99**, 016105.

79 I. C. Man, H. Y. Su, F. Calle-Vallejo, H. A. Hansen, J. I. Martínez, N. G. Inoglu, J. Kitchin, T. F. Jaramillo, J. K. Nørskov and J. Rossmeisl, *ChemCatChem*, 2011, **3**, 1159.

80 G. Jones, T. Bligaard, F. Abild-Pedersen and J. K. Nørskov, *J. Phys. Condens. Matter*, 2008, **20**, 064239.

81 E. Tayyebi, J. Hussain, Y. Abghoui and E. Skúlason, *J. Phys. Chem. C*, 2018, **122**, 10078.

82 A. B. Laursen, A. S. Varela, F. Dionigi, H. Fanchiu, C. Miller, O. L. Trinhammer, J. Rossmeisl and S. Dahl, *J. Chem. Educ.*, 2012, **89**, 1595.

83 M. Pourbaix, 1974, ISBN: 978-0915567980.

84 Gurudayal, J. Bullock, D. F. Srankó, C. M. Towle, Y. Lum, M. Hettick, M. C. Scott, A. Javey and J. Ager, *Energy Environ. Sci.*, 2017, **10**, 2222.

85 P. K. Jiwanti, A. M. Ichzan, R. K. P. Dewandaru, S. R. Atriardi, Y. Einaga and T. A. Ivandini, *Diam. Relat. Mater.*, 2020, **106**, 107874.

86 J. Horkans and M. W. Shafer, *J. Electrochem. Soc.*, 1977, **124**, 1202.

87 L. Li, Z.J. Zhao, C. Hu, P. Yang, X. Yuan, Y. Wang, L. Zhang, L. Moskaleva and J. Gong, *ACS Energy Lett.*, 2020, **5**, 552.

88 X. Li, L. Li, L. Wang, Q. Xia, L. Hao, X. Zhan, A. W. Robertson and Z. Sun, *Chem. Commun.*, 2022, **58**, 7412.

89 J. P. Hoare, *J. Electrochem. Soc.*, 1965, **112**, 1129.

90 Z. Li, Y. Feng, Y.L. Liang, C.Q. Cheng, C.K. Dong, H. Liu, W. Du, and Y.L. Liang, *Adv. Mater.*, 2020, **32**, 1908521.

91 Z. Li, Y. Ding, W. Kang, C. Li, D. Lin, X. Wang, Z. Chen, M. Wu and D. Pan, *Electrochim. Acta*, 2015, **161**, 40.

92 N. Sotani, K. Eda, M. Sadamatu and S. Takagi, 2006, **62**, 903.

93 J. Benedicto Hernandez, 2018, Master of Science dissertation, University of California .

94 M. Sarno and E. Ponticorvo, *Int. J. Hydrogen Energy*, 2017, **42**, 23631.

95 X. Peng, Y. Chen, Y. Mi, L. Zhuo, G. Qi, J. Ren, Y. Qiu, X. Liu and J. Luo, *Inorg. Chem.*, 2019, **58**, 8910.

96 P. Koltun, *Prog. Nat. Sci. Mater. Int.*, 2010, **20**, 16.

97 M. Suchea, S. Christoulakis, K. Moschovis, N. Katsarakis and G. Kiriakidis, *Thin Solid Films*, 2006, **515**, 551.

98 K. Sen Chou, T. K. Lee and F. J. Liu, *Sensors Actuators B Chem.*, 1999, **56**, 106.

99 Z. S. Macedo, R. S. Da Silva, M. E. G. Valerio and A. C. Hernandes, *Nucl. Inst. Methods Phys. Res. B*, 2004, **218**, 153.

100 J. Suntivich, K. J. May, H. A. Gasteiger, J. B. Goodenough and Y. Shao-Horn, *Science*, 2011, **334**, 1383.

101 E. Baktash, P. Littlewood, R. Schomäcker, A. Thomas and P. C. Stair, *Appl. Catal. B Environ.*, 2015, **179**, 122.

102 C. M. Rost, E. Sachet, T. Borman, A. Moballegh, E. C. Dickey, D. Hou, J. L. Jones, S. Curtarolo and J. P. Maria, *Nat. Commun.*, 2015, **6**, 1.

103 J. Gild, J. Braun, K. Kaufmann, E. Marin, T. Harrington, P. Hopkins, K. Vecchio and J. Luo, *J. Mater.*, 2019, **5**, 337.

104 P. Sarker, T. Harrington, C. Toher, C. Oses, M. Samiee, J. P. Maria, D. W. Brenner, K. S. Vecchio and S. Curtarolo, *Nat. Commun. 2018 91*, 2018, **9**, 1.

105 B. S. Murty, S. Ranganathan, J. W. Yeh and P. P. Bhattacharjee, 2019, 1, ISBN: 978-0128160671.

106 B. Cantor, I. T. H. Chang, P. Knight and A. J. B. Vincent, *Mater. Sci. Eng. A*, 2004, **375–377**, 213.

107 Z. Li, K. G. Pradeep, Y. Deng, D. Raabe and C. C. Tasan, *Nature*, 2016, **534**, 227.

108 S. S. Nene, M. Frank, K. Liu, S. Sinha, R. S. Mishra, B. A. McWilliams and K. C. Cho, *Scr. Mater.*, 2019, **166**, 168.

109 M. G. Poletti, G. Fiore, F. Gili, D. Mangherini and L. Battezzati, *Mater. Des.*, 2017, **115**, 247.

110 Y. F. Ye, Q. Wang, J. Lu, C. T. Liu and Y. Yang, *Mater. Today*, 2016, **19**, 349.

111 G. Anand, A. P. Wynn, C. M. Handley and C. L. Freeman, *Acta Mater.*, 2018, **146**, 119.

112 L. Tang, Z. Li, K. Chen, C. Li, X. Zhang and L. An, *J. Am. Ceram. Soc.*, 2021, **104**, 1953.

113 E. Alper and O. Yuksel Orhan, *Petroleum*, 2017, **3**, 109.

114 J. Ma, N. Sun, X. Zhang, N. Zhao, F. Xiao, W. Wei and Y. Sun, *Catal. Today*, 2009, **148**, 221.